Stem Cell Reports
Article
ISSCR
OPEN ACCESS

Pathogenic Pathways in Early-Onset Autosomal Recessive Parkinson's Disease Discovered Using Isogenic Human Dopaminergic Neurons

Tim Ahfeldt,[1,2,3,*] Alban Ordureau,[5] Christina Bell,[5] Lily Sarrafha,[3,4] Chicheng Sun,[6,7] Silvia Piccinotti,[6,7] Tobias Grass,[6,7] Gustavo M. Parfitt,[1,2,3] Joao A. Paulo,[5] Fumiki Yanagawa,[8] Takayuki Uozumi,[8] Yasujiro Kiyota,[8] J. Wade Harper,[5] and Lee L. Rubin[6,7,*]

[1]Nash Family Department of Neuroscience, Icahn School of Medicine at Mount Sinai, New York, NY 10029, USA
[2]Ronald M. Loeb Center for Alzheimer's Disease, Icahn School of Medicine at Mount Sinai, New York, NY 10029, USA
[3]Black Family Stem Cell Institute, Icahn School of Medicine at Mount Sinai, New York, NY 10029, USA
[4]Graduate School Department of Cell, Developmental and Regenerative Biology, Icahn School of Medicine at Mount Sinai, New York, NY 10029, USA
[5]Department of Cell Biology, Harvard Medical School, Boston, MA 02115, USA
[6]Department of Stem Cell and Regenerative Biology, Harvard University, Cambridge, MA 02138, USA
[7]Harvard Stem Cell Institute, Harvard University, Cambridge, MA 02138, USA
[8]Nikon Corporation, Shinagawa Intercity Tower C, 2-15-3, Konan, Minato-ku, Tokyo 108-0075, Japan
*Correspondence: tim.ahfeldt@mssm.edu (T.A.), lee_rubin@harvard.edu (L.L.R.)
https://doi.org/10.1016/j.stemcr.2019.12.005

SUMMARY

Parkinson's disease (PD) is a complex and highly variable neurodegenerative disease. Familial PD is caused by mutations in several genes with diverse and mostly unknown functions. It is unclear how dysregulation of these genes results in the relatively selective death of nigral dopaminergic neurons (DNs). To address this question, we modeled PD by knocking out the PD genes *PARKIN* (*PRKN*), *DJ-1* (*PARK7*), and *ATP13A2* (*PARK9*) in independent isogenic human pluripotent stem cell (hPSC) lines. We found increased levels of oxidative stress in all PD lines. Increased death of DNs upon differentiation was found only in the *PARKIN* knockout line. Using quantitative proteomics, we observed dysregulation of mitochondrial and lysosomal function in all of the lines, as well as common and distinct molecular defects caused by the different PD genes. Our results suggest that precise delineation of PD subtypes will require evaluation of molecular and clinical data.

INTRODUCTION

Parkinson's disease (PD) is a chronic and progressive neurodegenerative disorder that disproportionally affects dopaminergic neurons (DNs) in the substantia nigra pars compacta (SNc) of the midbrain (Dauer and Przedborski, 2003; Uhl et al., 1985). Most PD cases are sporadic, and little is known about the cause of their disease. However, approximately 10% of PD patients have a family history of the disease (Thomas and Beal, 2007). Studies of sporadic, as well as familial, PD patients suggest that both are affected by the dysregulation of similar biochemical pathways—most prominently, impairment of protein and mitochondrial homeostasis and oxidative stress (OS) (Chai and Lim, 2013).

A better understanding of the familial forms of PD could help elucidate pathways that are also relevant for the sporadic forms of the disease. Approximately 3%–5% of sporadic PD cases can be linked to mutations in one of six genes. Among these, mutations in the E3 ubiquitin ligase, *PARKIN*, the PTEN-induced putative kinase 1 (*PINK1*), the protein deglycase, *DJ-1*, and the presumptive cation-transporting ATPase 13A2 (*ATP13A2*) are inherited in an autosomal recessive fashion and cause completely penetrant early-onset PD in homozygous or compound heterozygous carriers (Klein and Westenberger, 2012). *PARKIN*-, *PINK1*-, and *DJ-1*-related forms of PD are clinically indistinguishable from each other in their pathology (Schulte and Gasser, 2011). In contrast, mutations in *ATP13A2* cause Kufor-Rakeb syndrome, an atypical presentation of PD involving additional symptoms of dementia, spasticity, and supranuclear gaze palsy (Hampshire et al., 2001; Paisan-Ruiz et al., 2010). The symptomatologies of these recessive mutations suggest that their study *in vitro* will reveal relevant common, but also distinct, dysregulated pathways for PD.

Advances in gene-editing technology of human pluripotent stem cells (hPSCs) allow studies of familial PD genes compared with isogenic controls. For example, *LRRK2* (Reinhardt et al., 2013), *SNCA* (Ryan et al., 2013), *PARKIN* (Shaltouki et al., 2015; Tabata et al., 2018), and *DJ-1* (Burbulla et al., 2017) mutations have been studied in this way. Although these studies have demonstrated PD-specific phenotypes such as OS, dopamine oxidation, and cell death, we still know little of the shared common or distinct mechanisms that accompany the pathological dysregulation.

Using CRISPR-Cas9 genome editing we developed isogenic loss-of-function models of early-onset autosomal recessive PD (PARKIN$^{-/-}$, DJ1$^{-/-}$, and ATP13A2$^{-/-}$) with the aim of identifying common and distinct elements of each. We combined our isogenic models with a knockin fluorescent reporter at the tyrosine hydroxylase (TH) locus that enabled isolation of large numbers of DNs. We further

This is an open access article under the CC BY-NC-ND license (http://creativecommons.org/licenses/by-nc-nd/4.0/).

developed an efficient 3D-spin reactor differentiation protocol to generate DNs on a large-scale in a reproducible fashion that allows studies in organoids/spheres and in a 2D format after dissociation.

These technical advances allowed us to carry out comparative quantitative global proteomic and transcriptomic analyses with the goal of identifying dysregulated pathways that contribute to the development of PD. Our characterization of the three isogenic PD lines revealed increased OS in the basal state in all mutant types of DNs with early specific loss of these neurons in the *PARKIN*$^{-/-}$ line. Using Ingenuity Pathway Analysis (IPA) and Kyoto Encyclopedia of Genes and Genomes (KEGG) analysis of transcriptomic and proteomic data, we identified subtype-specific dysregulation of PD-relevant pathways including changes in mitochondrial and lysosomal properties, and apoptosis.

RESULTS

Generation of Isogenic TH Knockin Reporter PD Cell Lines

The *TH* gene, encoding the rate-limiting enzyme in dopamine synthesis, is commonly used in immunocytochemistry experiments to quantify the percentage of DNs derived from hPSCs. We engineered a TH-p2a-Td:Tomato (red fluorophore protein) construct as a reporter for TH expression. We used a CRISPR-Cas9 genome editing strategy that relies on positive selection and CRE-mediated excision of the selection cassette to introduce this fluorescent reporter into the *TH* gene locus (Figure 1A). The targeting vector retained a largely unaltered endogenous *TH* gene product (Shaner et al., 2004) (Figures 1B and S1A). We used GFP labeling to enrich cultures that were successfully nucleofected with the CRE-GFP plasmid (Figure S1B). Correct knockin/homologous recombination events were determined through genotyping and DNA sequencing (Figures S1C and S1D). Knockin efficiency across three cell lines, determined by 5′ genotyping PCR, was 60%.

hPSC Differentiation into Midbrain DNs in 3D-Spin Reactors

Culture in 3D-spin reactors is scalable and less variable than standard organoid methods, allowing the production of hundreds of millions of cells per spin reactor (Amit et al., 2011; Qian et al., 2016; Rigamonti et al., 2016). To recapitulate midbrain differentiation (Kriks et al., 2011) we used dual-SMAD inhibition, followed by patterning via modulation of sonic hedgehog (SHH) and WNT signaling (Figure 1C). 2D cultures of hPSCs readily formed spheres after transfer into spin reactors and had a relatively homogeneous appearance. Differentiation of WA01-TH cells was initiated when pluripotent spheres reached an average diameter of 500 μm; that time point was named d0. During differentiation, spheres continuously increased in size. The average sphere diameter was 726 μm at d15, 784 μm at d22, and 1,119 μm at d38 (Figures 1D and S1E, left).

Virtually all cells comprising the spheres at d0 were positive for the pluripotency markers Tra-1-60 and OCT4 (Figure 1E, top). OCT4 and TRA-1-60 expression rapidly decreased and only a few cells were positive at d15. FOXA2 is one of the earliest genes to be expressed in the floor plate of the developing midbrain. After the midbrain patterning at d15, >95% of cells were positive for FOXA2 (Figure 1E, bottom left). Expression of the roof plate marker LMX1A appeared clustered on the edges of the neural progenitor cell (NPC) spheres. LMX1A and FOXA2 expression was absent in pluripotent spheres. Most cells remained FOXA2^{+} over the course of differentiation, but the staining appeared weaker at later time points. Staining with antibodies against TH and dsRed revealed the presence of a low percentage of TH:TdTomato-positive (TH^{+}) NPCs and early neurons at d15 (Figure 1E, bottom right). The TH percentage rapidly increased up to d22. At d38, about 40% of all cells stained positive for dsRed and TH. Similar differentiation efficiencies were noted in three independent wild-type (WT) hPSC lines that were tested.

The sphere size was also reproducible, as indicated by three independent differentiation experiments (Figures 1F and S1E, right). In differentiating spheres, we observed parallel tracks of axons on the outside, while the inside appeared less organized. To reveal 3D morphology and reporter fluorescence intensity, we took live cell images of d22 spheres derived from BJ-SIPS-TH-WT cells. The maximum intensity projection of 12 images shows bright fluorescent cell bodies with DN morphology, networks of neuronal processes and bright red puncta with regular and spherical appearance (Figure 1G). After differentiation, spheres could be dissociated using a gentle enzymatic digestion protocol.

We sorted cells based on TH:TdTomato expression. Positive neurons were plated on primary mouse glial cells. About 50% of TH^{+} neurons survived digestion and flow sort, and quickly grew processes. The sorted cells showed the characteristic morphology of hPSC-derived midbrain DNs. The TH:TdTomato reporter appeared very bright in live cultures but was noticeably dimmer after paraformaldehyde fixation. Cells were stained using antibodies against TH and dsRed: 98% of TH^{+} cells were also positive for dsRed. We did not observe cells that were dsRed^{+} but not TH^{+} (Figures 1H and S1F).

Isogenic Cell Lines Carrying Three Distinct PD Mutations

We used CRISPR editing to create isogenic PD lines from WT donor control cell lines (Figure 2A). We created CRISPR

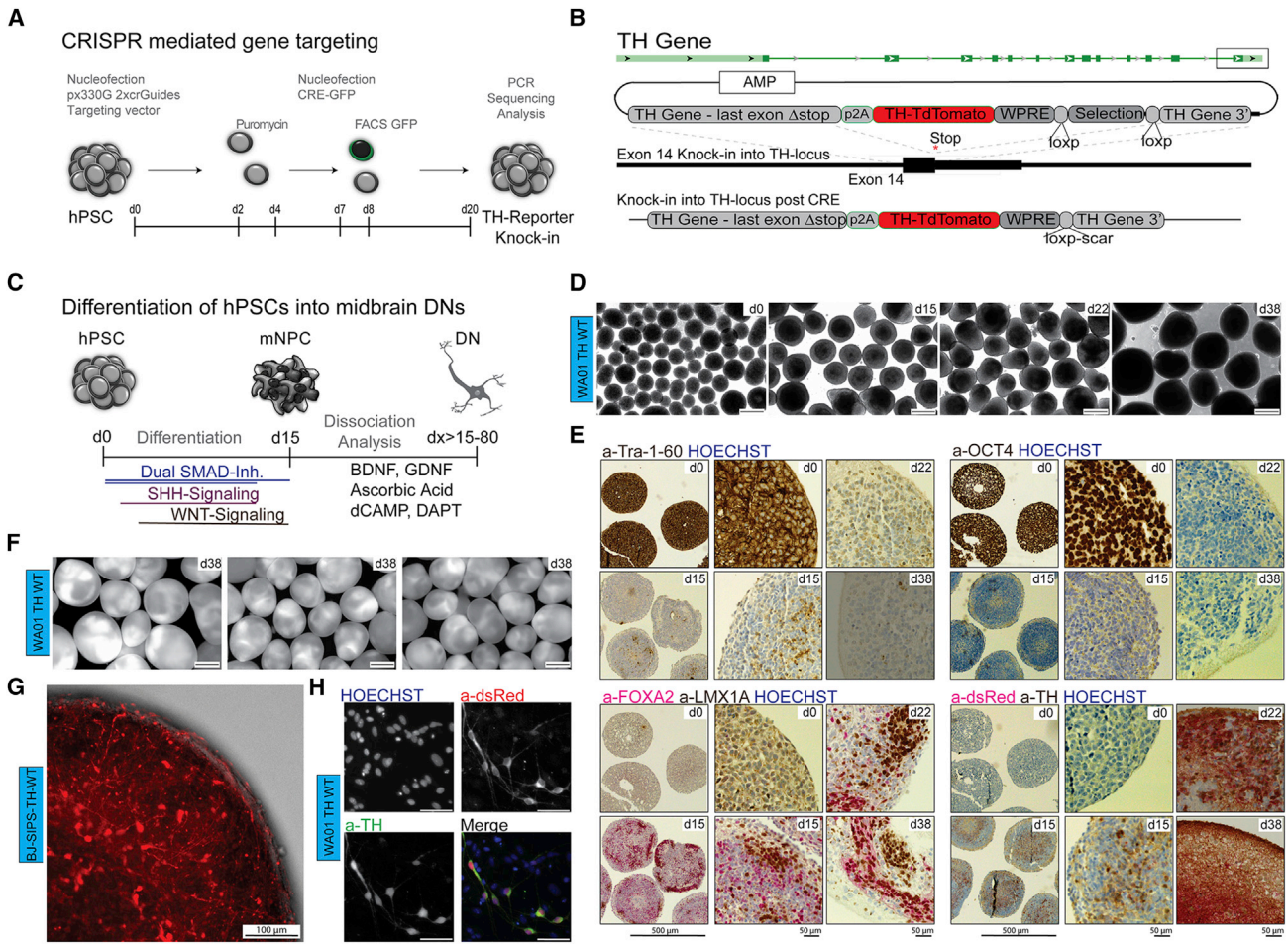

Figure 1. Spin Culture Differentiation of TH Reporter hPSCs into Midbrain DNs

(A) Experimental scheme depicting the CRISPR-mediated TH reporter knockin strategy.

(B) Donor plasmid containing the targeting vector *TH* with a 5′TH homology arm followed by a 2A self-cleaving peptide sequence, a WPRE sequence, floxed selection cassette, and 3′ TH homology arm. Genomic locus indicating the targeting area in exon 14 of the *TH* gene, red star representing the position of the stop codon. Schematic representation of successful targeting post-CRE excision.

(C) Experimental scheme showing the culture conditions in spin culture.

(D) Bright-field images of WA01-WT spheres at time points d0, d15, d22, and d38. Scale bars, 500 µm (4×).

(E) Immunohistochemistry of sectioned organoids/spheres. Each panel organized as (top left, 4× d0; bottom left, 4× d15. Scale bar, 500 µm (4×); top middle, 20× d0; bottom middle, 20× d15; top right, 20× d22; and bottom right, 20× d38. Scale bar, 50 µm (20×) using validated antibodies against: top left panel (TRA-1-60), top right panel (OCT4), bottom left panel (FOXA2 and LMX1A), and bottom right panel (dsRed and TH). Nuclei were counterstained using HOECHST.

(F) Fluorescence images of WA01-WT spheres at d38 showing TH:TdTomato reporter expression. Scale bars, 500 µm, 4× (n = 3 differentiation experiments).

(G) Maximum projection image of d22 sphere from differentiated BJ-SIPS WT TH cells showing TH:TdTomato expression. z stack images acquired using spinning disc confocal CX7 at 10×. Scale bar, 100 µm.

(H) Fluorescence microscopy panel, showing DNs at d38 from WA01-TH-WT cell lines, dissociated on d25 and plated in low density on glial cells. Scale bars, 50 µm, 20× (top left, Hoechst; top right, a-dsRed; bottom left, a-TH [MAB318]; bottom right, merge).

guides based on a px330-p2A-GFP variant designed to cause double-strand breaks in the coding regions of three distinct PD loci: *PARKIN*, *DJ-1*, and *ATP13A2* (Figure 2B). Flow sorting of GFP expression was used to enrich for successfully nucleofected cells (Figure S2A). We generated several PD clones in both HUES1 and WA01 cell lines. Edited clones were identified via PCR genotyping and Sanger sequencing (Figures S2B–S2D). Cell lines used in the study are listed (Figure 2C). We differentiated PD and control cell lines using a 3D-spin protocol. Analyzed clones exhibited a

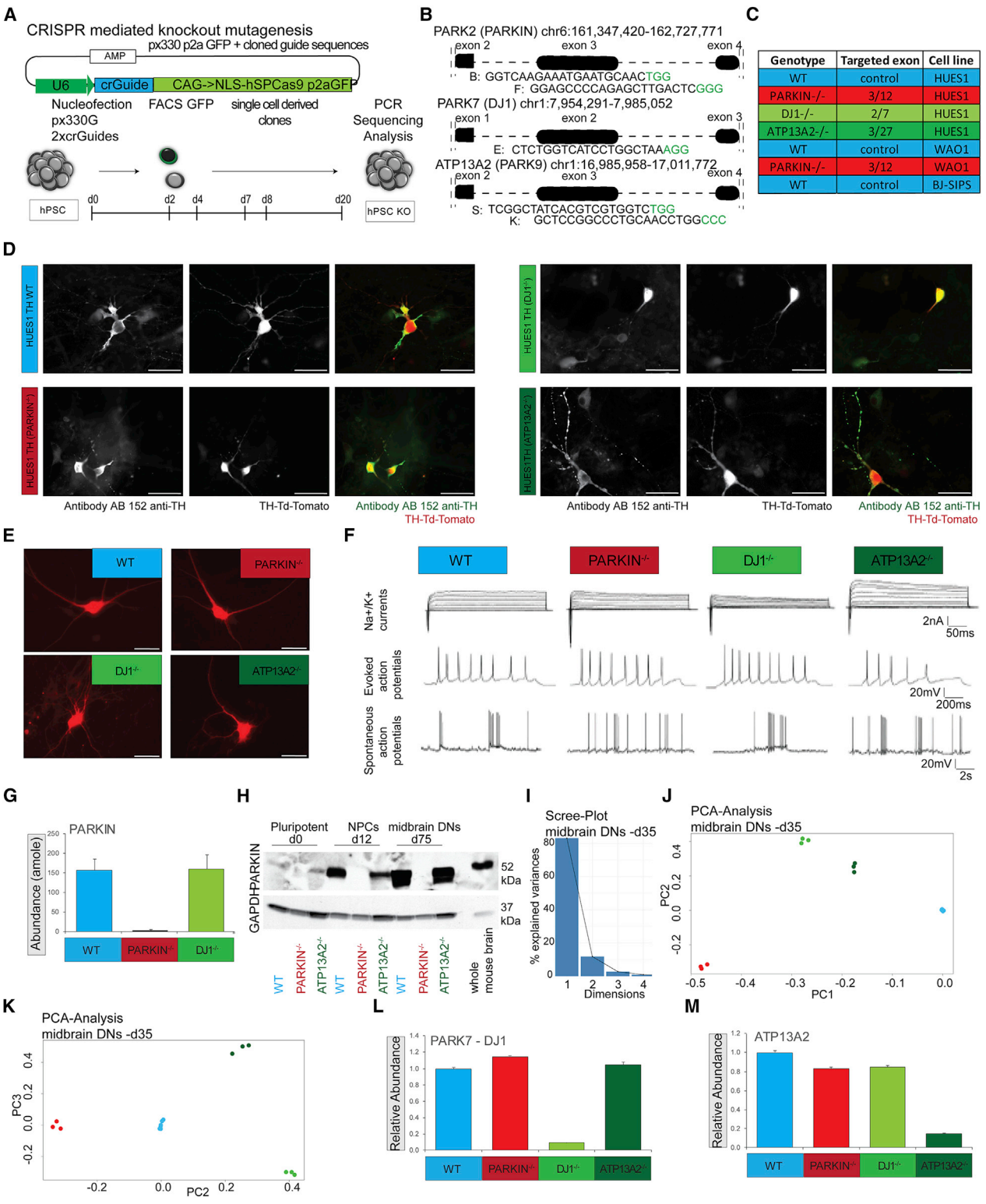

Figure 2. Generation, and Molecular and Functional Characterization of Knockout Cell Lines in the PD Model

(A) Experimental Scheme depicting the CRISPR knockout mutagenesis strategy.

(B) Graphical display of chromosome positions, targeted exons, and CRISPR sequences.

(legend continued on next page)

small cytoplasm to nucleus ratio and stained positive for the pluripotency markers TRA-1-60 and OCT4 (Figures S3A and S3B). Normal karyotypes were found in the WA01-TH-WT, BJ-SIPS-TH-WT, as well as WA01-TH-PARKIN clones that were analyzed (Figure S3C). DNs from all isogenic lines were isolated by fluorescence flow cytometry at various times (Figure S3D). Sorted DNs were cultured on mouse glial cells for up to 2 months.

To ensure that the reporter expression did not change, we co-stained reporter-expressing cells with an anti-TdTomato/RFP antibody. In all analyzed cell lines and clones, we detected strong overlap between the two antibody stains. There were only a few instances of cells that were positive to an anti-TH antibody and not positive using anti-dsRed antibody (Figures 2D and S1F). TdTomato was expressed diffusely throughout the cell body and less strongly within neuronal projections. The TH^+ neurons from all isogenic cell lines generally showed multipolar soma, elaborate dendrites, and axons (Figure 2E). Midbrain DNs exhibit two characteristic firing patterns, single spikes and bursting (Shi, 2005). To confirm that the hPSC-derived $TdTomato^+$ neurons were functionally consistent with their putative identification as DNs, we carried out electrophysiological measurements. We detected voltage-gated sodium and potassium currents, evoked repetitive action potentials, and frequent spontaneous potentials in TH:TdTomato DNs derived from both WT and isogenic PD lines (Figure 2F). Furthermore, live cell calcium imaging also showed spontaneous tetrodotoxin-sensitive activity in neurons from all the lines (Figure S3Ei-iii). Thus, all isogenic lines differentiated into functional DNs with electrophysiological properties similar to those described previously (Jiang et al., 2012; Kriks et al., 2011).

To confirm loss of the PARKIN protein we used isotope-labeled peptides (AQUA peptides) as an internal standard to allow absolute quantification of PARKIN in those samples (Ordureau et al., 2018; Stemmann et al., 2001). PARKIN was detected in both the WT and $DJ^{-/-}$ cell lines and was not detectable above background in the $PARKIN^{-/-}$ cell line (Figure 2G). A time course western blot analysis of PARKIN protein expression during differentiation showed complete loss of PARKIN at all developmental time points. PARKIN protein abundance increased substantially during differentiation in both WT and $ATP13A2^{-/-}$ lines (Figures 2H and S3F). We also confirmed loss of PARKIN in several WA01 clones (Figure S3G). In addition, using western blot techniques, we confirmed loss of DJ-1 in several HUES1 clones (Figure S3H).

Proteomics Reveals Global Differences between WT and Isogenic PD Cell Lines

To profile proteome alterations quantitatively in the isogenic PD lines, we used multiplexed tandem mass tag (TMT)-based quantitative mass spectrometry. We performed comparative studies between all cell lines in the pluripotent state as well as in d35 DNs, for which we generated differentiation triplicates. We quantified >7,000 proteins in 4 experiments for all the d35 DN samples. Comparative studies were conducted on a smaller intersection subset of >4,000 high-abundance proteins. All abundances, measured normalized relative abundances and fold changes, including statistical testing, are summarized in Table S1.

Principal-component analysis (PCA) performed on the d35 DN dataset showed strong reproducibility between independent differentiation replicates. A Scree plot shows that most variance in the dataset is represented by three components (Figure 2I). The first, second, and third components explain 83.1%, 11.8%, and 2.6% of the variance, respectively. A PCA plot of components 1 and 2 shows

(C) Table summarizing knockouts indicating targeted exons, and coloring scheme used in this study in isogenic HUES1, WA01 and BJ-SIPS lines: WT, $PARKIN^{-/-}$, $DJ\text{-}1^{-/-}$, and $ATP13A2^{-/-}$.
(D) Fluorescence microscopy panel, showing HUES1-derived DNs at d35 from all isogenic reporter cell lines, dissociated on d25 and plated in low density on mouse glial cells. Scale bars, 100 μm, 40× (left, ICC stained with TH antibody AB152; middle, TH:TdTomato reporter fluorophore expression, right merge).
(E) Fluorescence microscopy images of flow sorted TH^+ neurons from all isogenic lines 4 weeks post plating on glial cells before electrophysiological analysis. Scale bars, 50 μm.
(F) Whole-cell patch clamp recordings in TH^+-labeled DNs derived from all four iPSC lines (n = 6–9 for each line) showing voltage-gated sodium and potassium currents (top row), evoked action potentials (middle), and spontaneous action potentials (bottom).
(G) Quantification of PARKIN abundance in DNs from WT, $PARKIN^{-/-}$, and $DJ\text{-}1^{-/-}$ lines using AQUA peptides.
(H) Western blot of WT, $PARKIN^{-/-}$, and $ATP13A2^{-/-}$ lines using PARKIN antibody and GAPDH as a control, at three time points, indicated as pluripotent at d0, NPC at d12, midbrain DN at d75, and mouse whole-brain lysate as control.
(I) Scree plot showing the percentage of variances explained by each principal component.
(J) PCA plot of components 1 and 2 at d35.
(K) PCA plot of components 2 and 3 at d35.
(L) Bar chart showing normalized relative abundance of DJ1 protein, WT samples set to 1.
(M) Bar chart showing normalized relative abundance of ATP13A2 protein, WT samples set to 1. Statistical significance was analyzed by one-way ANOVA followed by post hoc test (1% FDR)-Bonferroni-Holm for multiple comparisons.

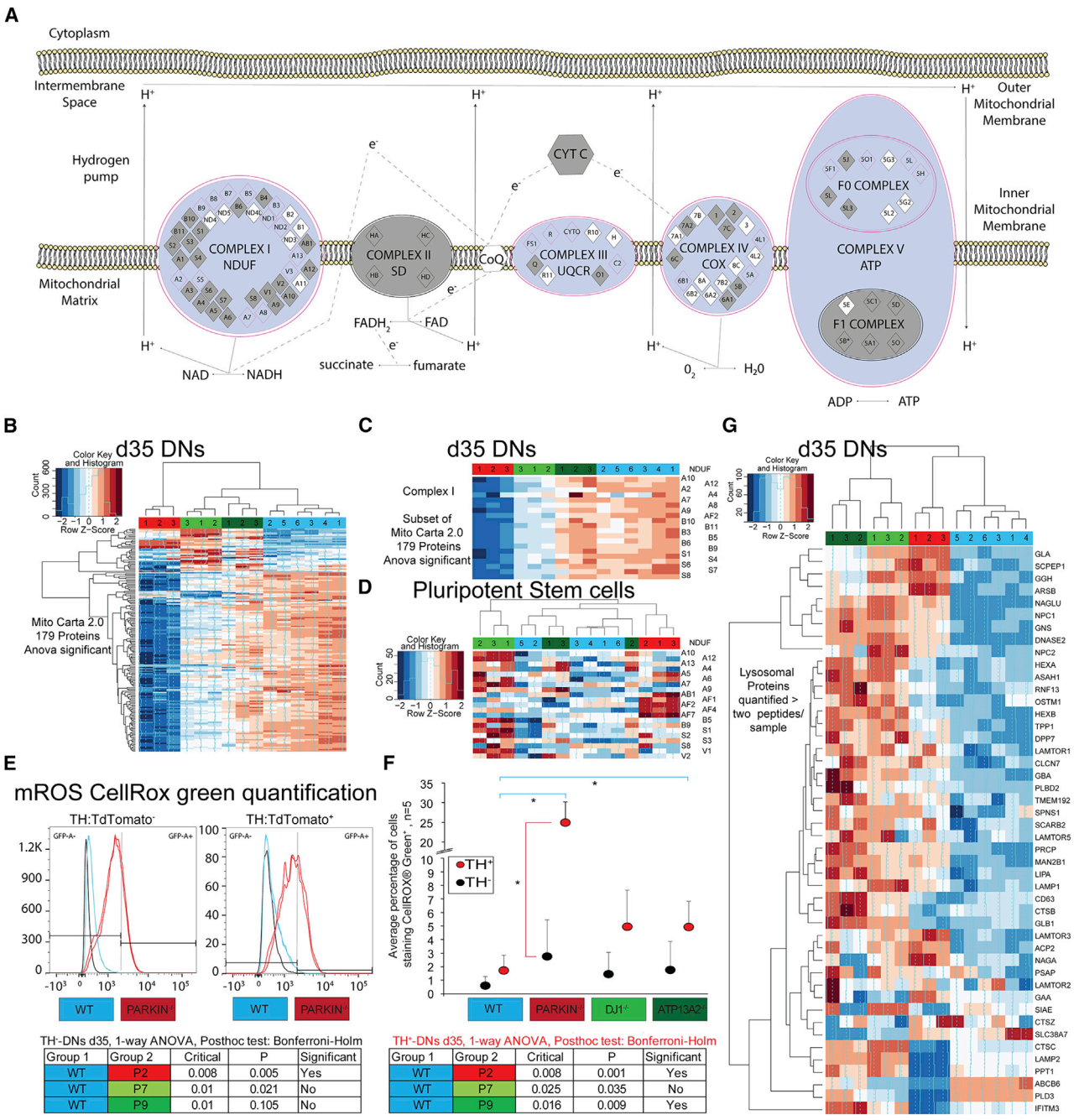

TH-DNs d35, 1-way ANOVA, Posthoc test: Bonferroni-Holm

Group 1	Group 2	Critical	P	Significant
WT	P2	0.008	0.005	Yes
WT	P7	0.01	0.021	No
WT	P9	0.01	0.105	No

TH+-DNs d35, 1-way ANOVA, Posthoc test: Bonferroni-Holm

Group 1	Group 2	Critical	P	Significant
WT	P2	0.008	0.001	Yes
WT	P7	0.025	0.035	No
WT	P9	0.016	0.009	Yes

Figure 3. OS, Mitochondrial Dysfunction and Lysosomal Dysregulation Are Shared Phenotypes in all Early-Onset PD DNs

(A) The canonical oxidative phosphorylation pathway created using IPA software. $\log_2$ fold changes were plotted. Purple outlines indicate significantly dysregulated proteins/pathways (based on −0.7/0.7 $\log_2$ fold change). Red color indicates a positive change or protein enrichment in the PARKIN$^{-/-}$ line (none noted), while blue represents a depletion.

(B, D, G) Heatmap.2 function across all samples using specified gene lists, default clustering and row scaling. Columns represent samples, rows represent genes, and color intensity represents column *Z* score, where red indicates enriched and blue depleted proteins.

(B) Heatmap analysis of 179 Mito Carta 2.0 proteins with mitochondrial function or localization that shows differential protein abundance between any cell line in d35 DNs.

(C) Subset of Mito Carta 2.0 analysis showing all quantified proteins that are part of the NDUF-complex I in d35 DNs.

(D) Heatmap of all proteins that were quantified with at least two unique peptides that are part of the NDUF-complex I in hPSCs.

(legend continued on next page)

distinct clusters that group samples by genotype, with component 1 separating WT from all isogenic DN lines, while component 2 separates the PARKIN$^{-/-}$ line from the DJ-1$^{-/-}$ and ATP13A2$^{-/-}$ lines (Figure 2J). PCA plots of components 2 and 3 show that component 3 separates the DJ-1$^{-/-}$ and ATP13A2$^{-/-}$ lines (Figure 2K). Three dimensions were sufficient to differentiate all samples by genotype. The variance in the hPSC lines was much smaller. However, loss of PARKIN led to its separation from all other cell lines through component 1 (Figures S4A–S4C). Analysis of differential protein abundance confirmed knockout of the DJ-1 and ATP13A2 proteins (Figures 2L and 2M).

PD Gene Loss Depletes Mitochondrial Proteins and Increases OS in TH$^+$ DNs

Postmortem brain analyses of PD patients, as well as of PD animal models, show increased OS through mitochondrial dysfunction in DNs as a common feature of PD pathology (Dias et al., 2013). Mitochondrial dysfunction and especially loss of complex I activity have been investigated as part of sporadic and familial PD etiology. We performed IPA on the proteomics data to explore pathways that were dysregulated between WT and PD lines. Canonical IPA showed many dysregulated pathways between WT and PARKIN$^{-/-}$ cell lines. The top 3 most significant pathways in d35 DNs were oxidative phosphorylation, mitochondrial dysfunction, and the sirtuin-signaling pathway (Figure S4D). These pathways were also dysregulated in pluripotent cells, but less significantly.

To determine dysregulation in pluripotent cells, we used significance cutoff adapted to the given dataset (from $\log_2$ fold change −0.7/0.7 in d35 DNs to −0.12/0.12 in d0 pluripotent cells). We overlaid the normalized protein abundance as fold changes between d35 DNs from WT and PARKIN$^{-/-}$ lines and mapped the proteins onto the canonical pathway "oxidative phosphorylation" obtained from IPA (Figure 3A). We observed significant depletion of mitochondrial proteins in complexes I, III, and IV. To examine mitochondrial dysfunction in all PD disease lines, we probed for proteins that were detected with at least two unique peptides that were classified as relevant to mitochondrial function (Mito Carta 2.0) and showed dysregulation using an ANOVA test. Heatmap analysis of the 179 dysregulated proteins showed global depletion of mitochondrial proteins in PARKIN$^{-/-}$ lines at d35 of differentiation (Figure 3B). However, subtle global depletion of mitochondrial proteins was noted in the other PD lines as well. We focused on a subset of these proteins, plotting only those that are part of complex I (NADH:ubiquinone oxidoreductase [NDUF] proteins). Complex I proteins were less abundant in the disease lines at d35 (Figure 3C), but not in d0 hPSCs (Figure 3D). Loss of complex I function has been linked to increased OS levels.

OS might be connected to DN-specific cellular functions such as dopamine metabolism. We found significantly reduced TH protein expression at d35 in independent WA01-derived Parkin$^{-/-}$ cells in line with our observations of reduced numbers of TH$^+$ DNs (Figures S4F and S4G). We measured protein carbonyl content, which is considered a marker of oxidative modification of proteins and, therefore, of OS. We found that the quantity of carbonylated proteins in differentiating hPSCs increased over time and was significantly different between d17 and d35 (Figures S4H–S4J). To test the role of PD mutations in the regulation of mitochondrial reactive oxygen species (mROS), we analyzed the levels of mROS using the live cell dye CellROX Green and the TH:TdTomato reporter in all of the isogenic cell lines following differentiation (Figures 3E and 3F) and quantified the percentage of cells exhibiting high green fluorescence (mROS-G$^+$) in each population. PARKIN$^{-/-}$ cell lines showed significantly elevated levels of mROS in TH$^+$ DNs versus TH$^-$ cells (Figure 3F). WT control cell lines showed fewer mROS events than all PD cell lines. This difference was significant for comparison between WT control and ATP13A2$^{-/-}$ cell lines but was most severe as a consequence of loss of PARKIN (Figure 3F, blue arcs). Our data suggest that increased mROS and mitochondrial changes in DNs are part of a shared etiology.

PD Gene Loss Changes Lysosomal Function and Other PD-Relevant Pathways

Dysregulation of the autophagy-lysosomal pathway (ALP) is central to sporadic and familial PD pathology. We hypothesized that changes in protein abundance in the basal state without any perturbation of ALP would be an indicator for dysregulation of lysosomal function. We plotted proteins that were detected with at least two unique peptides and were annotated as part of the lysosomal

(E) Dissociated spheres at d35 were stained with CellROX green to detect mROS production in the basal state. mROS-G$^+$ was quantified in TH$^-$ as well as TH$^+$ cells. Histograms of mROS-G positivity overlaid with no staining control, stained WT (blue) and PARKIN$^{-/-}$ (red) lines, respectively.

(F) Averaged mROS percentage, quantified as mROS-G$^+$ using synchronized bisector gates (FloJo, LLC) to divide the x axis into GFP$^-$ and GFP$^+$ non-overlapping populations based on the background expression in our unstained control. Statistical significance was analyzed by one-way ANOVA followed by Bonferroni-Holm multiple comparison test (n = 4 independent staining and flow experiments significance indicated in tables [bottom]).

(G) Heatmap analysis of proteins with an annotated lysosomal function that were quantified with at least two unique peptides.

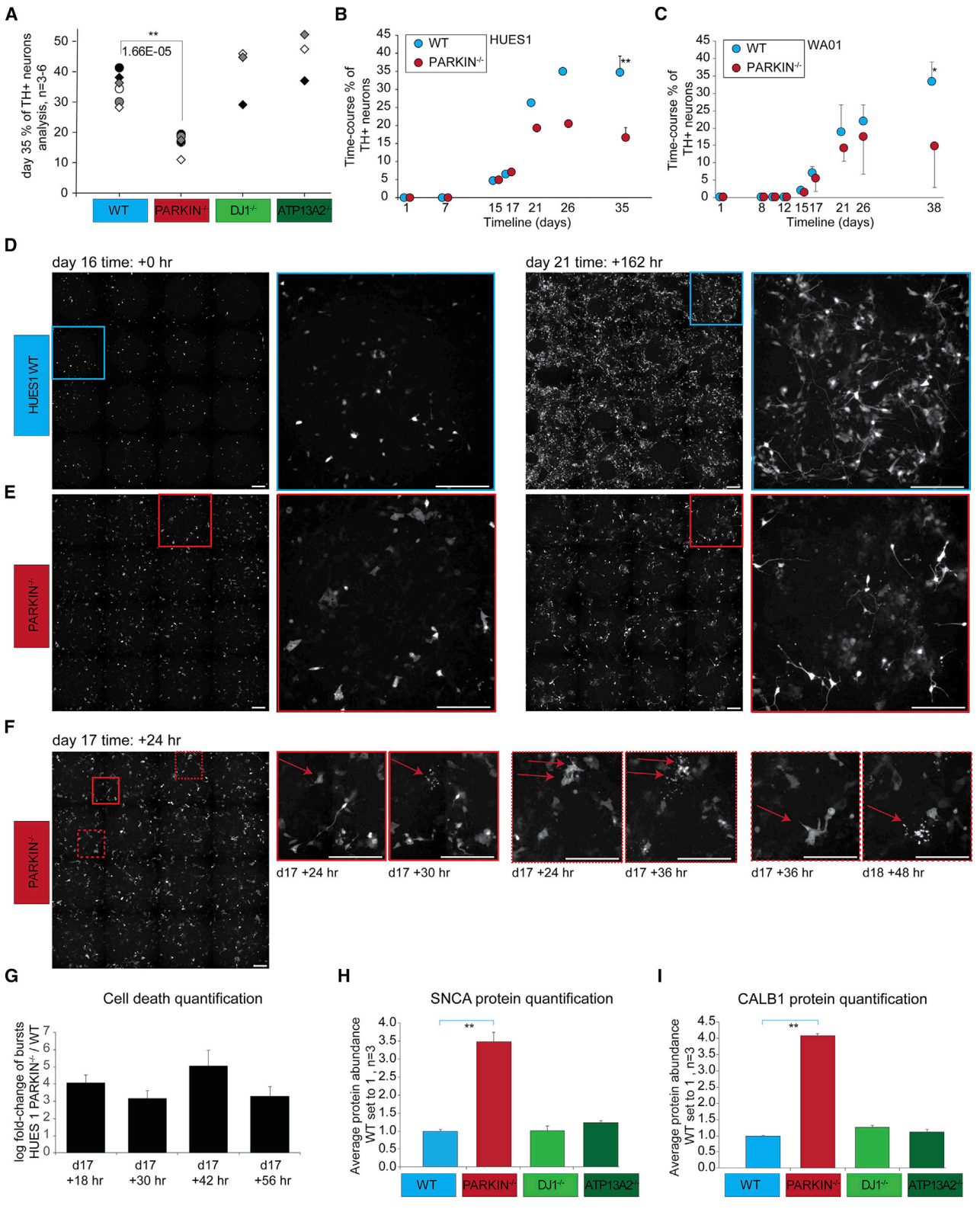

(legend on next page)

compartment. Heatmap analysis of the 46 proteins showed global enrichment of lysosomal proteins in both the ATP13A2$^{-/-}$ and DJ-1$^{-/-}$ cell lines. Dysregulation was also present in PARKIN$^{-/-}$, but hierarchical clustering revealed that the dysregulation was distinct from that of the other PD cell lines (Figure 3G). Thus, autophagy-lysosomal function and OS are commonly dysregulated pathways in PD and similarly appear dysregulated in DNs derived from the isogenic cell lines. It is unclear whether changes in the amount of lysosomal proteins resulted from increased induction or a block in completion of the autophagy process.

PARKIN Loss Causes Cell Death of Early TH$^+$ Neurons

Using IPA comparison analysis, we tested curated pathways for diseases and biological functions that were present in all WT versus PD line comparisons. We found dysregulation of pathways relevant to cellular function and maintenance, cell morphology, nervous system development and function, neurological disease, and cell death and survival (Figure S4E). Cell death and apoptosis can be triggered by excessive generation of free radicals, mitochondrial dysfunction, damage to DNA, or activation of lysosomal proteases. We hypothesized that the increase in OS in early-onset PD mutations could result in increased cell death rates in midbrain DNs in basal culture conditions. We dissociated spheres at different times during differentiation and analyzed the population for the percentage of TH$^+$ cells via fluorescence flow cytometry. The average percentage of TH$^+$ neurons in HUES1 WT, DJ-1$^{-/-}$, and ATP13A2$^{-/-}$ lines was ~40% at d35, indicating the absence of substantial changes in differentiation or survival of TH$^+$ neurons in these lines. However, we found that the TH$^+$ fraction was significantly smaller (16.7%) in the PARKIN$^{-/-}$ line at the same time point (Figure 4A). A time course of TH$^+$ neuron emergence showed no significant differences in the onset of reporter expression or the percentage of TH$^+$ cells during the first 17 days of differentiation in WT and PARKIN$^{-/-}$ lines (Figure 4B). We validated this finding using an independent WA01-TH cell line and three PARKIN$^{-/-}$ clones. Differences in TH percentage arose early and were significant at d38 of analysis (Figure 4C). Reduced differentiation or birth of DNs, as well as increased cell death, might have contributed to the smaller numbers of TH$^+$ cells in the PARKIN$^{-/-}$ cell lines.

To distinguish between reduced birth and increased death, we focused on the critical window between d15 and d21. We conducted a time-lapse experiment using an automated live cell imager (Nikon Biostation, CT) to examine the fate of newly generated TH$^+$ cells, as well as to track these cells over time, with the goal of determining whether the differences were due to differentiation or survival. We plated 50,000 unsorted cells per 0.32 cm^2 from HUES1 WT and PARKIN$^{-/-}$ isogenic cell lines on d15. We noted faint TH expression in WT-derived cells with either NPC morphology or immature neuron morphology without apparent neuritic processes (Figure 4D, left—overview and magnification). Over time, WT TH$^+$ cells gained in fluorescence intensity, grew processes, and exhibited a morphology typical of DNs (Figure 4D, right—overview and magnification). However, cells in the PARKIN$^{-/-}$ line behaved differently. At d16, 24 h post-dissociation, many of the faintly TdTomato-expressing cells showed increased vacuolation when compared with WT cells (Figure 4E, left—overview and magnification). At the end of the experiment at d21 the PARKIN$^{-/-}$ DNs exhibited typical morphology, but showed substantially reduced numbers and processes (Figure 4E, right—overview and magnification). During the course of the experiment we observed cell death in TH$^+$ cells in the PARKIN$^{-/-}$ line. Highly vacuolated cells burst and released fluorescent protein particles

Figure 4. Quantification of Cell Death Events in TH$^+$ DNs

(A) Dissociated spheres were analyzed via flow cytometry, TH quantification in isogenic HUES1 lines at d35 showing decreased numbers of TH$^+$ cells in the PARKIN$^{-/-}$ line. Statistical significance p value derived from one-way ANOVA followed by Bonferroni-Holm multiple comparison test (n = 6, 6, 3, and 3 independent differentiation experiments).

(B) TH quantification in WT and PARKIN$^{-/-}$ isogenic lines in a time course experiment in HUES1 line (n = 1 except d35 n = 6).

(C) TH quantification in WT and PARKIN$^{-/-}$ isogenic lines in a time course experiment in WA01 line (d0–d21, WT, n = 3 differentiation replicates; PARKIN$^{-/-}$, n = 3 independent clones; d26–d38, WT, n = 4 differentiation replicates; PARKIN$^{-/-}$, n = 5 or 3 independent clones, 2 differentiation replicates; d38, *p < 0.05, unpaired two-sided t test).

(D–F) Nikon Biostation CT live cell fluorescence imaging of TH:TdTomato expression during differentiation of WT and PARKIN$^{-/-}$ lines after dissociation at d15. Image acquisition starts 24 h post plating. Images were acquired every 6 h, time points indicated. Squares depict areas of interest that are shown in higher magnification. (D) WT cell line. (E) PARKIN$^{-/-}$ cell line. (F) Representative images of cell death events in the PARKIN$^{-/-}$ cell line. Zoomed images with red arrows indicating cells of interest before and after cell death.

(G) Cell death quantification of burst events in WT and PARKIN$^{-/-}$ cell lines at the indicated time points, shown as $\log_2$ fold change between PARKIN$^{-/-}$ and WT cell lines (n = 3 wells per cell line). *p < 0.05, unpaired two-sided t test.

(H) Bar chart showing normalized relative abundance of SNCA protein across all samples, WT samples set to 1.

(I) Bar chart showing normalized relative abundance of CALB1 protein across all samples. WT samples set to 1. Statistical significance was analyzed by one-way ANOVA followed by post hoc test (1% FDR) Bonferroni-Holm for multiple comparisons.

in small vacuoles that disappeared within 12–24 h (Figure 4F). The phenotype is clearly visible in Video S1. Over the course of the 5-day imaging period, many newly born TH^+ DNs disappeared from the culture, after displaying cellular fragmentation (Video S1). We observed significantly fewer such events in the WT cell line. Quantification revealed a 3–5 log fold increase of cell death events in $PARKIN^{-/-}$ TH^+ cells (Figure 4G).

Elevated levels of SNCA are sufficient to cause early-onset familial PD in a dose-dependent manner which leads to neuronal dysfunction. We observed significant (>3-fold) protein enrichment of SNCA in d35 $PARKIN^{-/-}$ DNs, but not in the other PD cell lines (Figure 4H). We hypothesized that hPSC-derived DNs represent a heterogeneous group of cells similar to the composition found in the human midbrain and that ventral tegmental area (VTA)-like neurons should be less affected by cell death than SNpc neurons. There are no molecular markers that can clearly delineate SNc from VTA, but calbindin (CALB1) is used in the field for its higher expression in the VTA (Bodea and Blaess, 2015). CALB1 protein abundance was >4-fold upregulated in the $PARKIN^{-/-}$ cell line, but not the other PD lines that did not exhibit cell death (Figure 4I).

Overlapping Dysregulated Genes and Pathways in $PARKIN^{-/-}$ and $ATP13A2^{-/-}$ Cell Lines

We generated RNA sequencing transcriptomics datasets from all isogenic HUES1 cell lines to identify common and distinct dysregulated genes and networks in the three isogenic PD lines in an unbiased manner, with the goal of grouping similar and distinct forms of PD. To minimize noise and capture signal only from DNs, d35 spheres were dissociated and TH^+ cells were purified by flow sorting for TdTomato expression. RNA sequencing profiles were generated in three separate differentiation experiments (n = 3) (Figure S5A). To visualize the relationship between each individual sample in our dataset, we performed unsupervised clustering as a multidimensional scaling plot, in which the distances correspond to leading log fold changes between each pair of RNA samples (Figures 5A and S5B). The plot revealed substantial differences between $PARKIN^{-/-}$ versus all other isogenic lines, which led to the separation by dimension 1. Dimension 2 separated biological replicate two from the other replicates. Dimension 3 separated the $ATP13A2^{-/-}$ line from the WT and $DJ\text{-}1^{-/-}$ lines. The $PARKIN^{-/-}$ line is the most dissimilar from all other lines.

We performed differential gene expression analysis and examined the results for overlap of genes and pathways. We identified genes that were differentially regulated by at least 2-fold, with a p value <0.01 between WT and all isogenic PD lines and validated genes via qRT-PCR (Figures 5B, top and S5C; Table S2). We conducted an overlap analysis to determine whether differentially expressed genes (DEGs) between WT and all isogenic disease lines were present in common pathways or were independent from one another (Figure 5B, bottom). Only six genes were differentially regulated in all three isogenic lines. We found 37 genes that were differentially expressed between $DJ\text{-}1^{-/-}$ and WT. However, among these, 24 were also differentially expressed in the $PARKIN^{-/-}$ lines. Shared genes were dysregulated in opposite directions, suggesting disparate disease mechanisms in $DJ\text{-}1^{-/-}$ compared with $PARKIN^{-/-}$ (Figure 5C). We found no significant dysregulated pathways in our KEGG pathway enrichment analysis of this comparison. In addition, 141 genes were differentially expressed between the $ATP13A2^{-/-}$ and WT lines. Of these, 64 were also differentially expressed between the $PARKIN^{-/-}$ and WT lines. The heatmap analysis demonstrated that in $PARKIN^{-/-}$ and $ATP13A2^{-/-}$ DNs, most expression changes had the same direction when compared with WT or $DJ\text{-}1^{-/-}$ DNs (Figure 5D).

To analyze the differential expression results in a network context, we performed IPA and independent KEGG pathway enrichment analysis on all DEGs between WT and isogenic PD lines. We found that the $PARKIN^{-/-}$ and $ATP13A2^{-/-}$ lines showed similar patterns of dysregulation. The two top KEGG pathways found dysregulated in both lines were hsa04512—extracellular matrix (ECM) receptor interaction; and hsa04974—protein digestion and absorption (Figure S5D). IPA of canonical pathways showed dysregulation of hepatic fibrosis, which is based on the dysregulation of ECM proteins, and axonal guidance signaling in all PD lines. Dysregulation of GABA (gamma-aminobutyric acid) receptor signaling was significant in the $PARKIN^{-/-}$ cell line, while calcium signaling was significant in both the $PARKIN^{-/-}$ and $ATP13A2^{-/-}$ cell lines (Figure 5E).

Altered Cellular Functions and DN Compositions in the $PARKIN^{-/-}$ Line

In addition to the commonly dysregulated KEGG pathways, we found several KEGG pathways with direct relevance to DNs that were significantly dysregulated only in the $PARKIN^{-/-}$ line. These pathways included hsa05032, morphine addiction; hsa04726, serotonergic synapse; hsa04727, GABAergic synapse; hsa05030, cocaine addiction; and hsa04080, neuroactive ligand-receptor interaction (Figure S5D). We plotted genes contributing to any addiction pathways in the KEGG analysis (path:hsa05032, path:hsa05031, path:hsa05034, and path:hsa05033) and visualized the contributing genes in a heatmap. The $PARKIN^{-/-}$ line formed a distinct cluster compared with the other isogenic lines, showing dysregulation of many transcripts with prominent roles in dopaminergic function (Figure S5E).

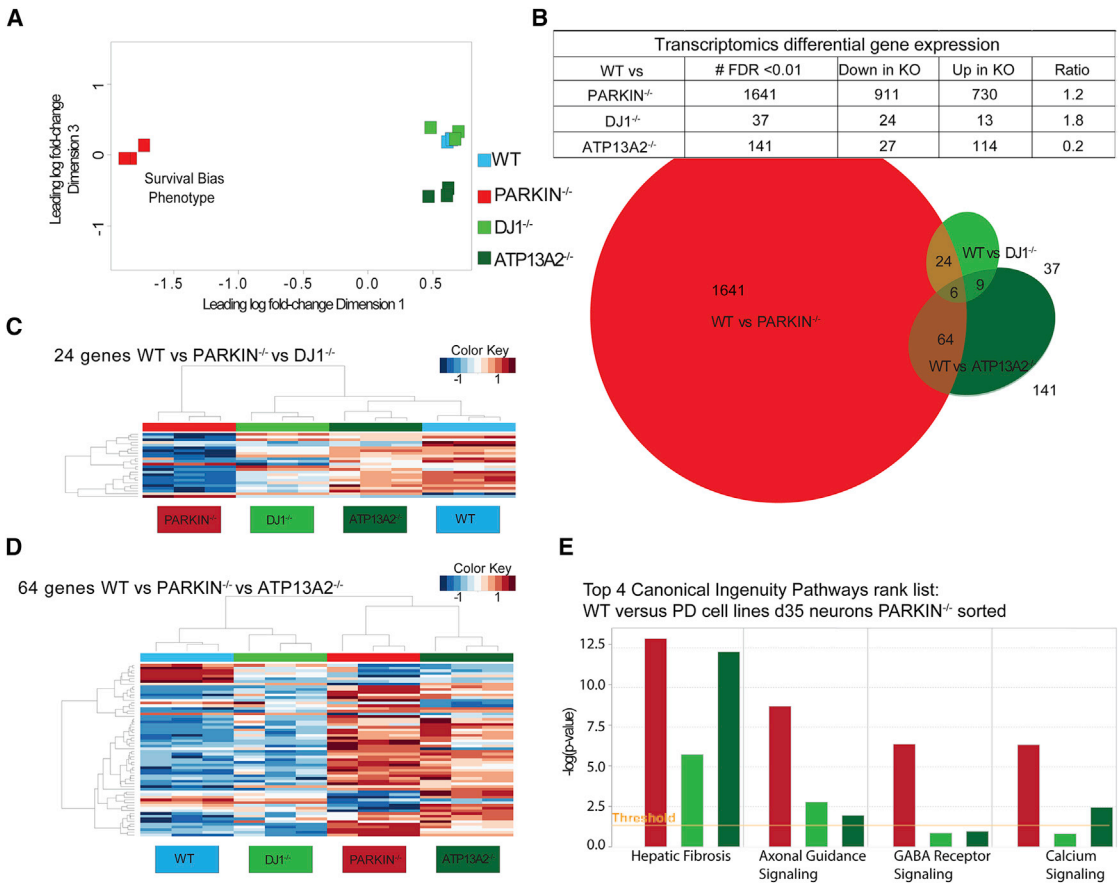

Figure 5. Transcriptomics Analysis of Sorted DNs Highlights Common and Distinct Dysregulation of PD-Relevant Genes and Pathways: HUES1 PD Lines

(A) Multidimensional scaling plot of all isogenic cell lines in which distance corresponds to leading log fold changes between each pair of RNA samples. Dimension 1 separates PARKIN$^{-/-}$ line from all other lines and dimension 3 separates the ATP13A2$^{-/-}$ line from WT and DJ-1$^{-/-}$ lines.

(B) Table showing the number of significant DEGs between WT and isogenic lines (FDR = 0.01), the number of up- and down-regulated genes, and the resulting ratio. Overlap analysis as a three-way Venn diagram intersecting DEGs between WT and all isogenic lines.

(C) Heatmap across all samples using the 24 intersecting genes between WT versus PARKIN$^{-/-}$ and WT versus DJ-1$^{-/-}$ analyses.

(D) Heatmap across all samples using the 64 intersecting genes between WT versus PARKIN$^{-/-}$ and WT versus ATP13A2$^{-/-}$ analyses.

(E) Bar chart of d35 global transcriptomics comparisons between WT and all PD cell lines showing select altered disease or biological function pathways determined using IPA curated sets. The y axis shows the significance (–log(p value)) and the orange line shows the significance threshold cutoff of −log(p value = 0.05), sorted by significance in PARKIN$^{-/-}$ versus WT comparison.

DISCUSSION

In this work, we have established and validated a robust large-scale 3D-spin culture protocol that allows for the derivation of midbrain DNs at high efficiency. We also generated an isogenic *in vitro* system to study cellular disease processes in WT and mutant DNs carrying severe autosomal recessive PD mutations in either *PARKIN*, *DJ-1*, or *ATP13A2*. We knocked in and validated a TH reporter to isolate relevant cells from our lines. Using our system, we have generated a deep proteomics dataset and analyzed the global protein abundance landscape across WT and PD disease lines. We further generated a transcriptomics dataset of sorted DNs from each of the lines. We found evidence of commonly dysregulated cellular functions involving OS and ALP. Dysregulation of PD-relevant pathways indicate shared and distinct molecular signatures among the isogenic PD cell lines. The PARKIN$^{-/-}$ lines were most distinct from controls and also were most distinct from the other PD lines. Identified shared or specific dysregulated candidate genes may inform efforts to find therapeutic targets and

to stratify PD pathology and patients on a molecular level.

3D-Spin Cultures for the Derivation of DNs

Most current protocols to derive midbrain DNs from hPSCs rely on dual-SMAD inhibition, and regulation of SHH and WNT signaling through growth factors or small molecules (Chambers et al., 2009; Kriks et al., 2011). To accommodate high input technologies—such as screening assays and proteomics analyses—we adapted and simplified the existing culture protocols (Chambers et al., 2009; Kriks et al., 2011) for use in large-scale spinner flask bioreactors. Our protocol is technically easy, fully defined, and shows high reproducibility and scalability for deriving large numbers of midbrain DNs. Immunocytochemistry was used to demonstrate midbrain-marker expression in NPCs and DNs. Transcriptomics and proteomics data showed the expected expression of dopaminergic genes and enzymes. Electrophysiology analysis revealed the presence of cells with properties typical of A9 type midbrain DNs, and reporter expression was highly correlated to staining with commercial TH antibodies. TH:TdTomato signal enabled fluorescence-activated cell sorting purification and allowed for live cell tracking and laser confocal microscopy 3D imaging of DN morphology. In addition, we developed a protocol that allows dissociation of 3D-derived neurons for culture on 2D dishes or coculture of isolated flow sorted neurons on glial cells. Spheres were maintained for up to 75 days, and there was no indication that the cultures cannot be maintained for longer time periods.

Omics Characterization of Isogenic PD Models

Protein stability and degradation are independent of transcriptional activity and strongly contribute to the regulation of protein levels. These processes are widely implicated in neurodegenerative diseases including PD (Caudle et al., 2010; Tai and Schuman, 2008). Here, we provide a comparative global molecular, functional, and phenotypic examination of several familial PD mutations in the same isogenic background. We generated transcriptomics data from sorted DNs and used quantitative proteomics to measure and quantify relative protein abundance in human DNs across our isogenic PD cell lines. PD is a disease of dysregulated proteins and accordingly we have linked PD genetics to emerging phenotypes in the relevant midbrain DNs and have established quantitative proteomics datasets (of >7,000 proteins) to explore genes, networks, and pathways that may contribute to PD etiology. High-confidence proteins were used for comparative studies. This deep quantitative proteomics dataset is a useful resource for the field and revealed common and distinct molecular dysregulation of PD cell lines and demonstrates the importance of studying PD in the relevant cell types.

OS and Mitochondrial Dysfunction Are Shared Phenotypes

There is evidence that OS is a component of the pathophysiology of familial and sporadic forms of PD. mROS are a source of cellular stress and have been examined in the context of PD and its hPSC models (Blesa et al., 2015; Cooper et al., 2012; Csobonyeiova et al., 2016; Dias et al., 2013). IPA of dysregulated proteins highlighted mitochondrial dysfunction, oxidative phosphorylation, and sirtuin-signaling pathways as the three most significant dysregulated pathways in the PARKIN$^{-/-}$ cell line. Despite the presence of antioxidants in the differentiation medium, analysis using flow cytometry revealed significantly increased levels of mROS in the basal state in all mutated lines when compared with the isogenic WT control. This increase was more pronounced in the TH^{+} cells, demonstrating the cell-type-specific vulnerability of DNs, further highlighting the utility of modeling PD in disease-relevant cells. Reduced activity of complex I, the NADH dehydrogenase complex, in mitochondria has been observed in midbrain tissue of sporadic PD patients (Keeney et al., 2006). Loss of PARKIN caused dysregulation of mitochondrial proteins in hPSCs, but the associated molecular dysregulation and measured phenotypes were significantly higher in the relevant DNs. This effect may be linked to dopamine oxidation, which is thought to initiate a toxic cascade that links OS to lysosomal dysfunction and SNCA aggregation (Burbulla et al., 2017).

The Interplay of Factors that May Explain Midbrain DN Phenotypes and Cell Death

SNCA was the first specific genetic aberration to have been linked to the development of PD (Polymeropoulos et al., 1997), and accumulation of SNCA aggregates and the formation of Lewy bodies are hallmarks of PD. SNCA was more than 3-fold enriched in PARKIN$^{-/-}$ DNs when compared with WT DNs.

PARKIN is broadly expressed throughout the body, including the heart, testis, liver, and kidney, as well as the brain (Kuhn et al., 2004). However, PD patients in general and those carrying loss-of-function PARKIN mutations exhibit the dysfunction and death of midbrain DNs. Parkin protein abundance was lowest in hPSCs and highest in DNs. Knockout mutations in the PARKIN gene resulted in a cell-type-specific phenotype culminating in the selective diminution of TH^{+} neurons in basal culture conditions. Using live cell time-lapse imaging and in association with a TH reporter we were able to show cellular phenotypes, such as enlarged vacuolated cell bodies and cell

death with fragmentation of cellular compartments in PARKIN$^{-/-}$ cell lines, reminiscent of paraptosis, paraptosis-like cell death, necroptosis, and some forms of lysosomal cell death, all of which are associated with strong cytoplasmic vacuolation and which can lead to a cell death phenotype that has been described as bursting (Aits and Jaattela, 2013; Shubin et al., 2016). Cell death occurs at a vulnerable stage, shortly after the onset of TH expression and the first synthesis of dopamine, when the cells are also undergoing major and energy-consuming morphological changes, neuron and neurite growth, and show increased SNCA expression.

Current protocols to derive midbrain DNs result in a heterogeneous mix of non-neuronal cells, DNs, and other neuronal cell types (Marton and Ioannidis, 2018). DNs themselves represent a heterogeneous group, containing SNc and VTA identities, among others (Xia et al., 2016). Midbrain DNs are anatomically separated into SNc and VTA. In PD patients, a subtype of nigral DNs shows enhanced vulnerability, while other populations, such as VTA DNs, are much less affected. Similarly, in our cultures, some, but not all, DNs died. CALB1 is often used as a marker to distinguish VTA from SN and shows higher expression in the VTA. VTA DNs also play a primary role in the reward system and addiction. Both increased CALB1 levels and the analysis of commonly dysregulated KEGG pathways in our PARKIN$^{-/-}$ cell lines point toward a shift in the surviving population and we speculate that hPSC-derived DNs model the specific vulnerabilities of DN subpopulations found in human brains. Pathway analysis of transcriptional data between WT and PARKIN$^{-/-}$ cell lines implicated dysregulation of both GABAergic synapse and reward systems.

Isogenic PD Models Reveal Common and Distinct Disease Pathways

Abnormal protein aggregation, OS/mitochondrial dysregulation and endoplasmic reticulum stress are critical pathological mechanisms involving ALP (Plotegher and Duchen, 2017). Most models of ALP rely on chemical perturbations to initiate or arrest the relevant cellular functions. In our isogenic PD lines, specific PD-associated mutations drove all measured differences. Analyzing proteomics data, we found that DJ1$^{-/-}$ and ATP13A2$^{-/-}$ cell lines showed similar dysregulation, while the PARKIN$^{-/-}$ line shows distinct dysregulation.

Overall, our experimental platform using a knockin fluorescence reporter in the *TH* locus, together with our results on phenotyping, transcriptomics, and proteomic analyses of isogenic lines, provide an improved understanding of *PARKIN*, *DJ-1*, and *ATP13A2* function. Our isogenic models allowed us to compare the impact of PD-relevant genes on the differentiation and health of the most vulnerable cell type in PD. Our study demonstrates how isogenic PD hPSCs can be used to understand PD-relevant disease pathology, determine affected pathways, and enhance our knowledge of genetic interactions in PD pathology. We have demonstrated DN-specific disease-relevant phenotypes in the PARKIN$^{-/-}$ line and identified OS as a common pathology and a shared dysregulated pathway in all isogenic cell lines. Conversely, and despite similar clinical presentations, we found evidence for at least two etiological PD subtypes, PARKIN$^{-/-}$ versus the ATP13A2$^{-/-}$and DJ-1$^{-/-}$ lines, indicating that precise delineation of PD subtypes will require evaluation of both molecular and clinical data.

EXPERIMENTAL PROCEDURES

See further details in the Supplemental Experimental Procedures.

Propagation and Maintenance of hPSCs

hESC line HUES01, from Harvard University (Cowan et al., 2004), was cultured on Matrigel-coated plates (ESC qualified, BD Biosciences) using hESC mTeSR-1 cell culture medium (STEMCELL Technologies) under conditions of 37°C, 95% air, and 5% CO_2 in a humidified incubator as described previously (Schinzel et al., 2011). The WA01 and BJ-SIPS cell lines were cultured on Geltrex-coated (100 μL matrix/10 mL basal medium) plates in StemFlex medium (Gibco) under the same conditions.

hPSC Adaption and Maintenance in Spinner Flasks

hPSCs were cultured in 125-mL disposable spinner flasks (Corning, VWR) on a nine-position stir plate (Dura-Mag) at a speed of 65 rpm, in a 37°C incubator with 5% CO_2, which is a higher speed than previously reported (Rigamonti et al., 2016). Before adaption to spinner flask culture, hPSCs were expanded in 10-cm dishes (Corning) until they reached confluence. Cells were dissociated using Accutase (Innovative Cell Technologies) for approximately 5 min at room temperature or until colonies detached from the plate. Cells were counted using a Bio-Rad automated cell counter. Forty million individual hPSCs were seeded into a spinner flask in 120 mL of StemFlex medium supplemented with 10 μM ROCK inhibitor Thiazovivin (STEMCELL Technologies). Spheres formed spontaneously, and, after 48 h, approximately half of the culture medium was replaced. The cells were maintained as undifferentiated pluripotent spheres in spin culture, with medium changes every other day until the spheres were approximately 500 μm (organoid area was measured using Nikon software in brightfield).

Differentiation into Midbrain DNs in Spin Culture

Differentiation was initiated through a full medium switch using differentiation medium d0. Subsequently medium was changed every other day by removing approximately 50% of the medium after spheres were allowed to settle by gravity. Differentiation medium to pattern toward midbrain has a changing composition outlined in experimental scheme in Figure 1 and contains DMEM-F12,

N2, B27, 10 μM transforming growth factor β inhibitor SB431542 (R&D Systems) and 100 nM BMP inhibitor LDN193189 (Stemgent) (dual-SMAD inhibition), 1 μM CHIR99021 (Stemgent), 2 μM purmorphamine (Stemgent or STEMCELL Technologies), and 1 μM SAG (Cursi or Cayman Chemical). Terminal differentiation medium contains 10 ng/mL brain-derived neurotrophic factor (R&D), 10 ng/mL glial cell line-derived neurotrophic factor (R&D), 0.2 mM ascorbic acid (Sigma), 0.1 mM butyryl cAMP (Sigma or Biolog), and 10 μM N-[N-(3,5-difluorophenacetyl)-L-alanyl]-S-phenylglycine t-butyl ester(Tocris or Cayman Chemical) (BAGTC).

Data Access

The accession number for the RNA sequencing data generated in this paper is GEO: GSE140076. Table S2 lists all quantified proteins as well as associated TMT reporter ion intensities used for quantitative analysis.

Statistical Analysis

If not otherwise stated, experiments were carried out in clonal isogenic cell lines in at least three differentiation experiments that were separated by time in culture. The experiments were not randomized. In other experiments three independent clonal lines were used. The investigators were not blinded during experiments and outcome assessment. Immunofluorescence experiments were repeated independently 2 times and at least 20 cells were analyzed from a single experiment. When analyzing immunohistochemistry staining data of sectioned spheres, several spheres were analyzed using sections representing outer, inner, and middle layers. Error bars are mostly presented as the means ± SD unless otherwise specified. Statistical comparisons between pairs were made using Student's t test. Statistical significance across multiple samples for proteomics data was determined using one-way ANOVA (artificial within groups variance was set to 1 and correction for multiple hypothesis testing was done by permutation-based false discovery rate [FDR 1%] followed by a post hoc test [1% FDR Bonferroni-Holm]), Statistical analysis for gene expression was performed using standard normalization and multiple comparison methods of the edgeR package or denoted in the Supplemental Information.

SUPPLEMENTAL INFORMATION

Supplemental Information can be found online at https://doi.org/10.1016/j.stemcr.2019.12.005.

AUTHOR CONTRIBUTIONS

T.A. and L.L.R. conceived of the experiments, supervised the experimental work and wrote the final manuscript. T.A. carried out most of the experiments and data analysis presented. A.O., C.B., J.A.P. and J.W.H. collected the proteomics data and contributed to the related data analysis and manuscript writing. L.S., S.P., T.G. and G.M.P. collected cell biological data, assisted in the data analysis and manuscript writing. C.S. performed and interpreted the electrophysiological characterization of all cell lines. F.Y., T.U. and Y.K. assisted with the acquisition, analysis and interpretation of live cell imaging data. All authors discussed the results, provided critical feedback and contributed to the final manuscript.

ACKNOWLEDGMENTS

The authors thank Geraldine Jowett and Aya Alame for technical help and discussions, Methodios Ximerakis for help with PARKIN antibody staining conditions, Rich Krolewski, Kathleen Pfaff, and Jane LaLonde for critical reading, Matt LaVoie for ideas and discussions, Claire Reardon, Abbie Groff, Chiara Gerhardinger, and John Rinn for their help in making RNA-sequencing libraries, generating the dataset, and alignments, as well as advice on the experimental design and analysis, Silvia Ionescu and Joyce LaVecchio from the HSCRB-HSCI Flow Cytometry Core for discussions and technical expertise sorting dissociated neurons, Christopher Bare from the Deans Flow Cytometry CoRE at Icahn School of Medicine, Mount Sinai for flow cytometry training, and Aaron Bell and Valeriy Borukhov from the Neuropathology Brain Bank at the Icahn School of Medicine at Mount Sinai for technical expertise in sectioning, staining, and imaging spheres. This work was supported by a generous gift to the Harvard Stem Cell Institute from the Elizabeth Miller fund, and grants from Nikon Corporation and Biogen. In addition, this work was supported by the Michael J. Fox Foundation, NIH grant R37NS083524, and the Ned Goodnow Fund to J.W.H., and by a postdoctoral fellowship from the Edward R. and Anne G. Lefler Center to A.O.

Received: November 7, 2017
Revised: December 4, 2019
Accepted: December 4, 2019
Published: January 2, 2020

REFERENCES

Aits, S., and Jaattela, M. (2013). Lysosomal cell death at a glance. J. Cell Sci *126*, 1905–1912.

Amit, M., Laevsky, I., Miropolsky, Y., Shariki, K., Peri, M., and Itskovitz-Eldor, J. (2011). Dynamic suspension culture for scalable expansion of undifferentiated human pluripotent stem cells. Nat. Protoc. *6*, 572–579.

Blesa, J., Trigo-Damas, I., Quiroga-Varela, A., and Jackson-Lewis, V.R. (2015). Oxidative stress and Parkinson's disease. Front Neuroanat. *9*, 91.

Bodea, G.O., and Blaess, S. (2015). Establishing diversity in the dopaminergic system. FEBS Lett. *589*, 3773–3785.

Burbulla, L.F., Song, P., Mazzulli, J.R., Zampese, E., Wong, Y.C., Jeon, S., Santos, D.P., Blanz, J., Obermaier, C.D., Strojny, C., et al. (2017). Dopamine oxidation mediates mitochondrial and lysosomal dysfunction in Parkinson's disease. Science *357*, 1255–1261.

Caudle, W.M., Bammler, T.K., Lin, Y., Pan, S., and Zhang, J. (2010). Using 'omics' to define pathogenesis and biomarkers of Parkinson's disease. Expert Rev. Neurother. *10*, 925–942.

Chai, C., and Lim, K.L. (2013). Genetic insights into sporadic Parkinson's disease pathogenesis. Curr. Genomics *14*, 486–501.

Chambers, S.M., Fasano, C.A., Papapetrou, E.P., Tomishima, M., Sadelain, M., and Studer, L. (2009). Highly efficient neural

conversion of human ES and iPS cells by dual inhibition of SMAD signaling. Nat. Biotechnol. *27*, 275–280.

Cooper, O., Seo, H., Andrabi, S., Guardia-Laguarta, C., Graziotto, J., Sundberg, M., McLean, J.R., Carrillo-Reid, L., Xie, Z., Osborn, T., et al. (2012). Pharmacological rescue of mitochondrial deficits in iPSC-derived neural cells from patients with familial Parkinson's disease. Sci. Transl. Med. *4*, 141ra190.

Cowan, C.A., Klimanskaya, I., McMahon, J., Atienza, J., Witmyer, J., Zucker, J.P., Wang, S., Morton, C.C., McMahon, A.P., Powers, D., et al. (2004). Derivation of embryonic stem-cell lines from human blastocysts. N. Engl. J. Med. *350*, 1353–1356.

Csobonyeiova, M., Danisovic, L., and Polak, S. (2016). Induced pluripotent stem cells for modeling and cell therapy of Parkinson's disease. Neural Regen. Res. *11*, 727–728.

Dauer, W., and Przedborski, S. (2003). Parkinson's disease: mechanisms and models. Neuron *39*, 889–909.

Dias, V., Junn, E., and Mouradian, M.M. (2013). The role of oxidative stress in Parkinson's disease. J. Parkinsons Dis. *3*, 461–491.

Hampshire, D.J., Roberts, E., Crow, Y., Bond, J., Mubaidin, A., Wriekat, A.L., Al-Din, A., and Woods, C.G. (2001). Kufor-Rakeb syndrome, pallido-pyramidal degeneration with supranuclear upgaze paresis and dementia, maps to 1p36. J. Med. Genet. *38*, 680–682.

Jiang, H., Ren, Y., Yuen, E.Y., Zhong, P., Ghaedi, M., Hu, Z., Azabdaftari, G., Nakaso, K., Yan, Z., and Feng, J. (2012). Parkin controls dopamine utilization in human midbrain dopaminergic neurons derived from induced pluripotent stem cells. Nat. Commun. *3*, 668.

Keeney, P.M., Xie, J., Capaldi, R.A., and Bennett, J.P., Jr. (2006). Parkinson's disease brain mitochondrial complex I has oxidatively damaged subunits and is functionally impaired and misassembled. J. Neurosci. *26*, 5256–5264.

Klein, C., and Westenberger, A. (2012). Genetics of Parkinson's disease. Cold Spring Harb. Perspect. Med. *2*, a008888.

Kriks, S., Shim, J.W., Piao, J., Ganat, Y.M., Wakeman, D.R., Xie, Z., Carrillo-Reid, L., Auyeung, G., Antonacci, C., Buch, A., et al. (2011). Dopamine neurons derived from human ES cells efficiently engraft in animal models of Parkinson's disease. Nature *480*, 547–551.

Kuhn, K., Zhu, X.R., Lubbert, H., and Stichel, C.C. (2004). Parkin expression in the developing mouse. Brain Res. Dev. Brain Res. *149*, 131–142.

Marton, R.M., and Ioannidis, J.P.A. (2018). A comprehensive analysis of protocols for deriving dopaminergic neurons from human pluripotent stem cells. Stem Cells Transl. Med. *8*, 366–374.

Ordureau, A., Paulo, J.A., Zhang, W., Ahfeldt, T., Zhang, J., Cohn, E.F., Hou, Z., Heo, J.M., Rubin, L.L., Sidhu, S.S., et al. (2018). Dynamics of PARKIN-dependent mitochondrial Ubiquitylation in induced neurons and model systems revealed by Digital Snapshot proteomics. Mol. Cell *70*, 211–227.e8.

Paisan-Ruiz, C., Guevara, R., Federoff, M., Hanagasi, H., Sina, F., Elahi, E., Schneider, S.A., Schwingenschuh, P., Bajaj, N., Emre, M., et al. (2010). Early-onset L-dopa-responsive parkinsonism with pyramidal signs due to ATP13A2, PLA2G6, FBXO7 and spatacsin mutations. Mov. Disord. *25*, 1791–1800.

Plotegher, N., and Duchen, M.R. (2017). Crosstalk between lysosomes and mitochondria in Parkinson's disease. Front. Cell Dev. Biol. *5*, 110.

Polymeropoulos, M.H., Lavedan, C., Leroy, E., Ide, S.E., Dehejia, A., Dutra, A., Pike, B., Root, H., Rubenstein, J., Boyer, R., et al. (1997). Mutation in the alpha-synuclein gene identified in families with Parkinson's disease. Science *276*, 2045–2047.

Qian, X., Nguyen, H.N., Song, M.M., Hadiono, C., Ogden, S.C., Hammack, C., Yao, B., Hamersky, G.R., Jacob, F., Zhong, C., et al. (2016). Brain-region-specific organoids using mini-bioreactors for modeling ZIKV exposure. Cell *165*, 1238–1254.

Reinhardt, P., Schmid, B., Burbulla, L.F., Schondorf, D.C., Wagner, L., Glatza, M., Hoing, S., Hargus, G., Heck, S.A., Dhingra, A., et al. (2013). Genetic correction of a LRRK2 mutation in human iPSCs links parkinsonian neurodegeneration to ERK-dependent changes in gene expression. Cell stem cell *12*, 354–367.

Rigamonti, A., Repetti, G.G., Sun, C., Price, F.D., Reny, D.C., Rapino, F., Weisinger, K., Benkler, C., Peterson, Q.P., Davidow, L.S., et al. (2016). Large-scale production of mature neurons from human pluripotent stem cells in a three-dimensional suspension culture system. Stem Cell Reports *6*, 993–1008.

Ryan, S.D., Dolatabadi, N., Chan, S.F., Zhang, X., Akhtar, M.W., Parker, J., Soldner, F., Sunico, C.R., Nagar, S., Talantova, M., et al. (2013). Isogenic human iPSC Parkinson's model shows nitrosative stress-induced dysfunction in MEF2-PGC1alpha transcription. Cell *155*, 1351–1364.

Schinzel, R.T., Ahfeldt, T., Lau, F.H., Lee, Y.K., Cowley, A., Shen, T., Peters, D., Lum, D.H., and Cowan, C.A. (2011). Efficient culturing and genetic manipulation of human pluripotent stem cells. PLoS One *6*, e27495.

Schulte, C., and Gasser, T. (2011). Genetic basis of Parkinson's disease: inheritance, penetrance, and expression. Appl. Clin. Genet. *4*, 67–80.

Shaltouki, A., Sivapatham, R., Pei, Y., Gerencser, A.A., Momcilovic, O., Rao, M.S., and Zeng, X. (2015). Mitochondrial alterations by PARKIN in dopaminergic neurons using PARK2 patient-specific and PARK2 knockout isogenic iPSC lines. Stem Cell Reports *4*, 847–859.

Shaner, N.C., Campbell, R.E., Steinbach, P.A., Giepmans, B.N., Palmer, A.E., and Tsien, R.Y. (2004). Improved monomeric red, orange and yellow fluorescent proteins derived from *Discosoma* sp. red fluorescent protein. Nat. Biotechnol. *22*, 1567–1572.

Shi, W.X. (2005). Slow oscillatory firing: a major firing pattern of dopamine neurons in the ventral tegmental area. J. Neurophysiol. *94*, 3516–3522.

Shubin, A.V., Demidyuk, I.V., Komissarov, A.A., Rafieva, L.M., and Kostrov, S.V. (2016). Cytoplasmic vacuolization in cell death and survival. Oncotarget *7*, 55863–55889.

Stemmann, O., Zou, H., Gerber, S.A., Gygi, S.P., and Kirschner, M.W. (2001). Dual inhibition of sister chromatid separation at metaphase. Cell *107*, 715–726.

Tabata, Y., Imaizumi, Y., Sugawara, M., Andoh-Noda, T., Banno, S., Chai, M., Sone, T., Yamazaki, K., Ito, M., Tsukahara, K., et al. (2018). T-type calcium channels determine the vulnerability of

dopaminergic neurons to mitochondrial stress in familial Parkinson disease. Stem Cell Reports *11*, 1171–1184.

Tai, H.C., and Schuman, E.M. (2008). Ubiquitin, the proteasome and protein degradation in neuronal function and dysfunction. Nat. Rev. Neurosci. *9*, 826–838.

Thomas, B., and Beal, M.F. (2007). Parkinson's disease. Hum. Mol. Genet. *16 Spec No. 2*, R183–R194.

Uhl, G.R., Hedreen, J.C., and Price, D.L. (1985). Parkinson's disease: loss of neurons from the ventral tegmental area contralateral to therapeutic surgical lesions. Neurology *35*, 1215–1218.

Xia, N., Zhang, P., Fang, F., Wang, Z., Rothstein, M., Angulo, B., Chiang, R., Taylor, J., and Reijo Pera, R.A. (2016). Transcriptional comparison of human induced and primary midbrain dopaminergic neurons. Sci. Rep. *6*, 20270.

Stem Cell Reports, Volume *14*

Supplemental Information

Pathogenic Pathways in Early-Onset Autosomal Recessive Parkinson's Disease Discovered Using Isogenic Human Dopaminergic Neurons

Tim Ahfeldt, Alban Ordureau, Christina Bell, Lily Sarrafha, Chicheng Sun, Silvia Piccinotti, Tobias Grass, Gustavo M. Parfitt, Joao A. Paulo, Fumiki Yanagawa, Takayuki Uozumi, Yasujiro Kiyota, J. Wade Harper, and Lee L. Rubin

Supplemental Figure 1

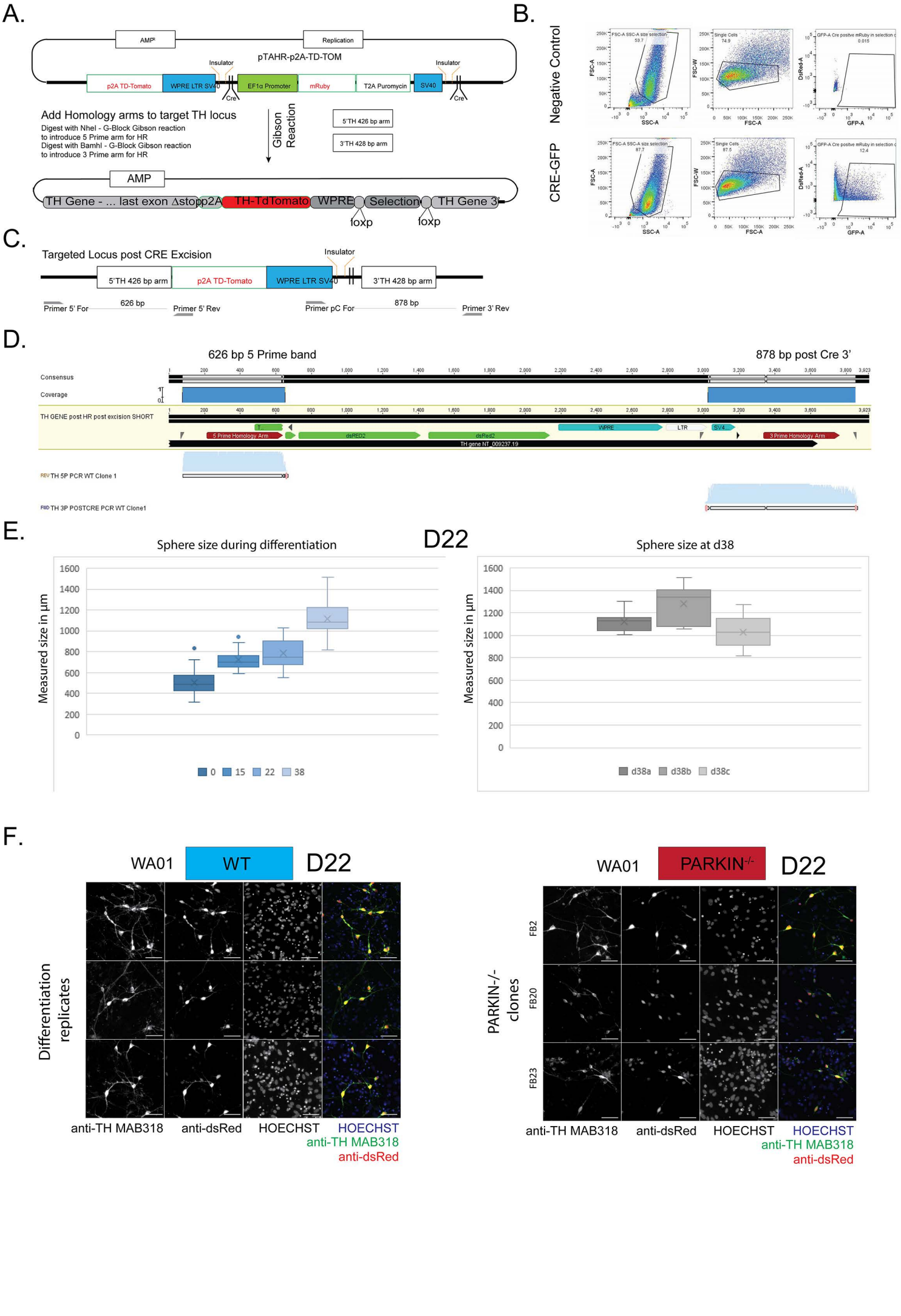

Supplemental Figure 2

A.

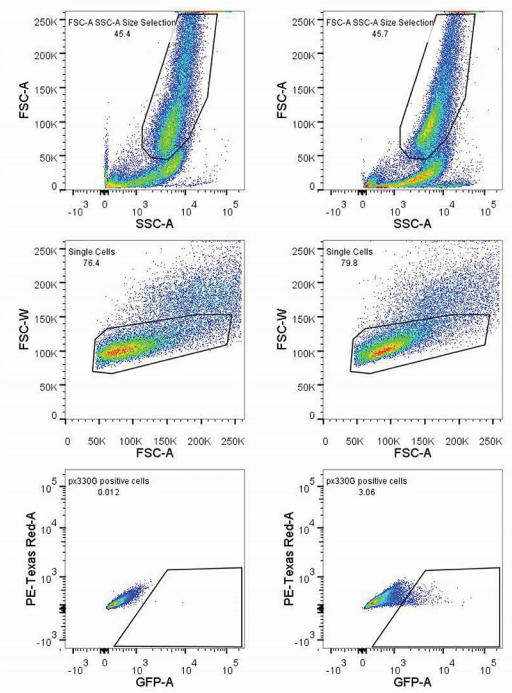

B.

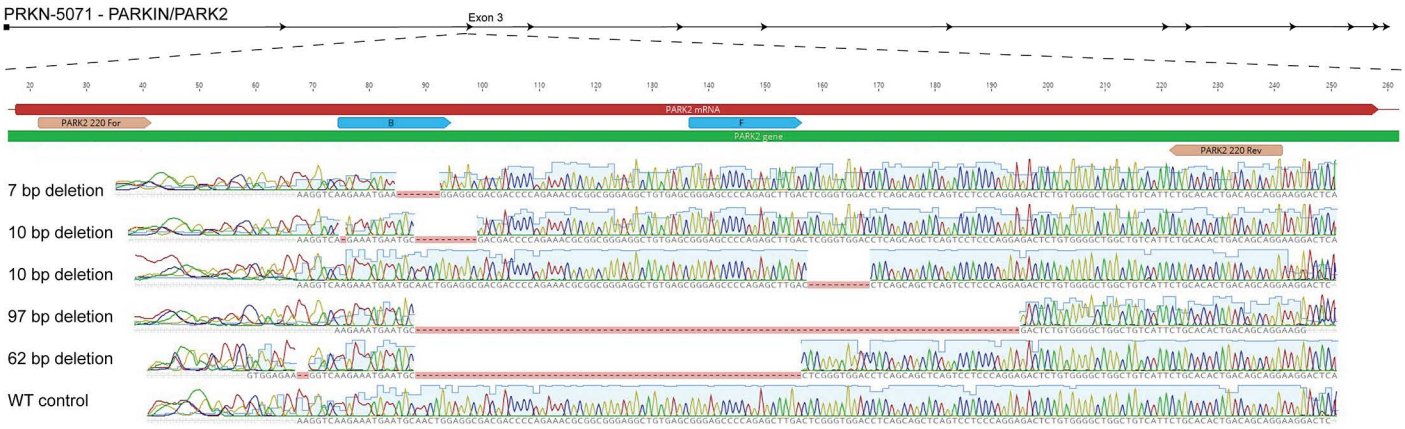

C.

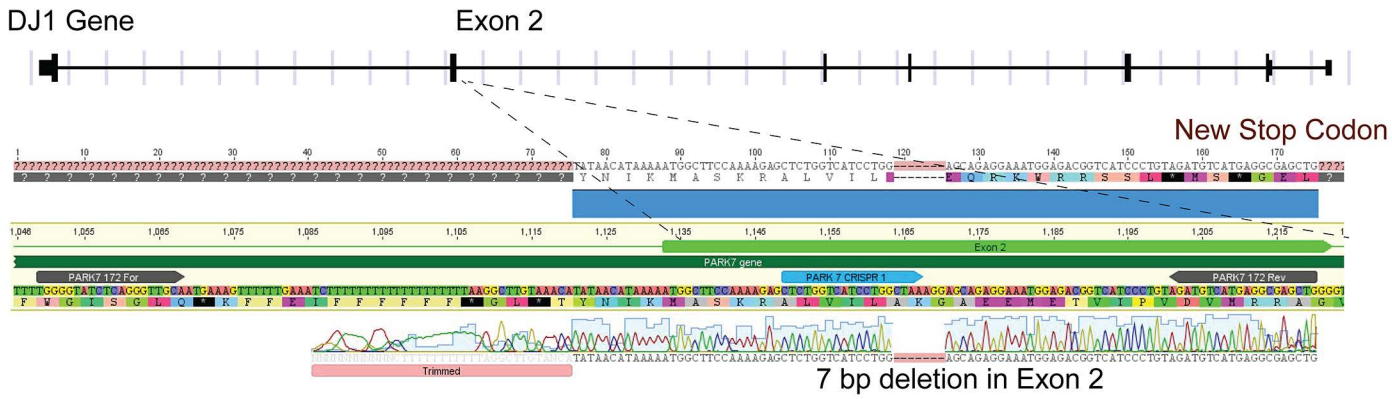

D.

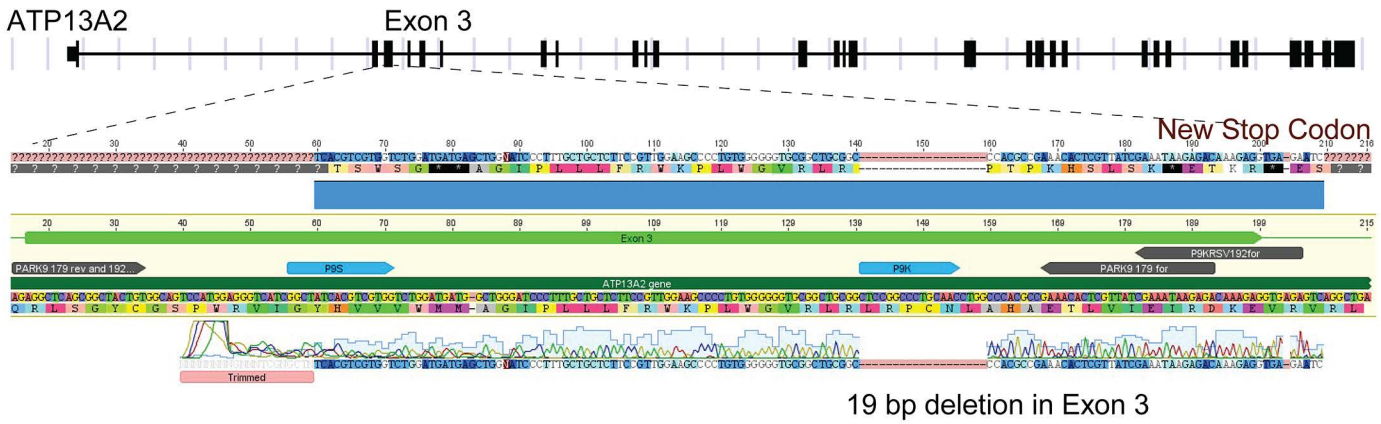

Supplemental Figure 3

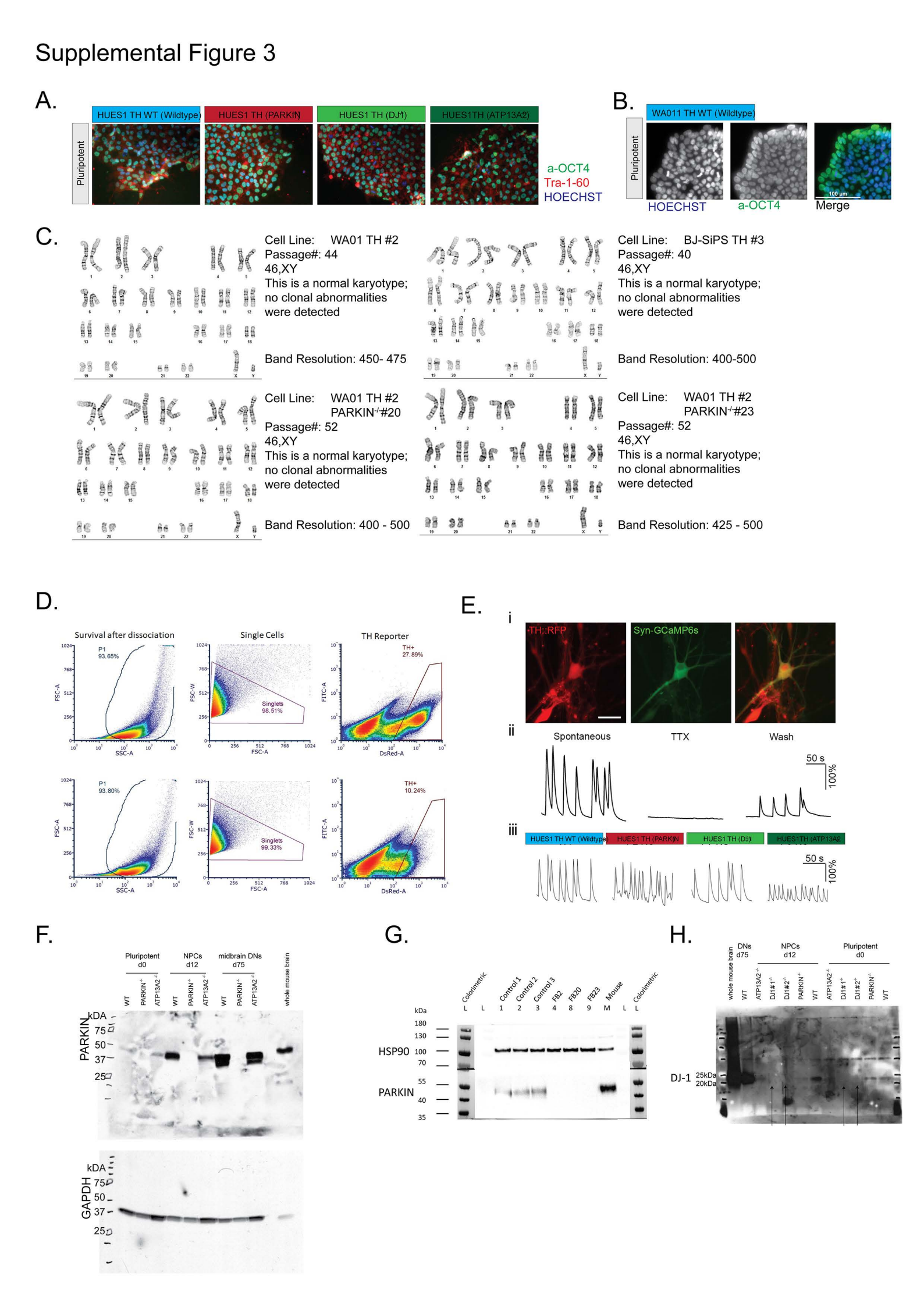

Supplemental Figure 4

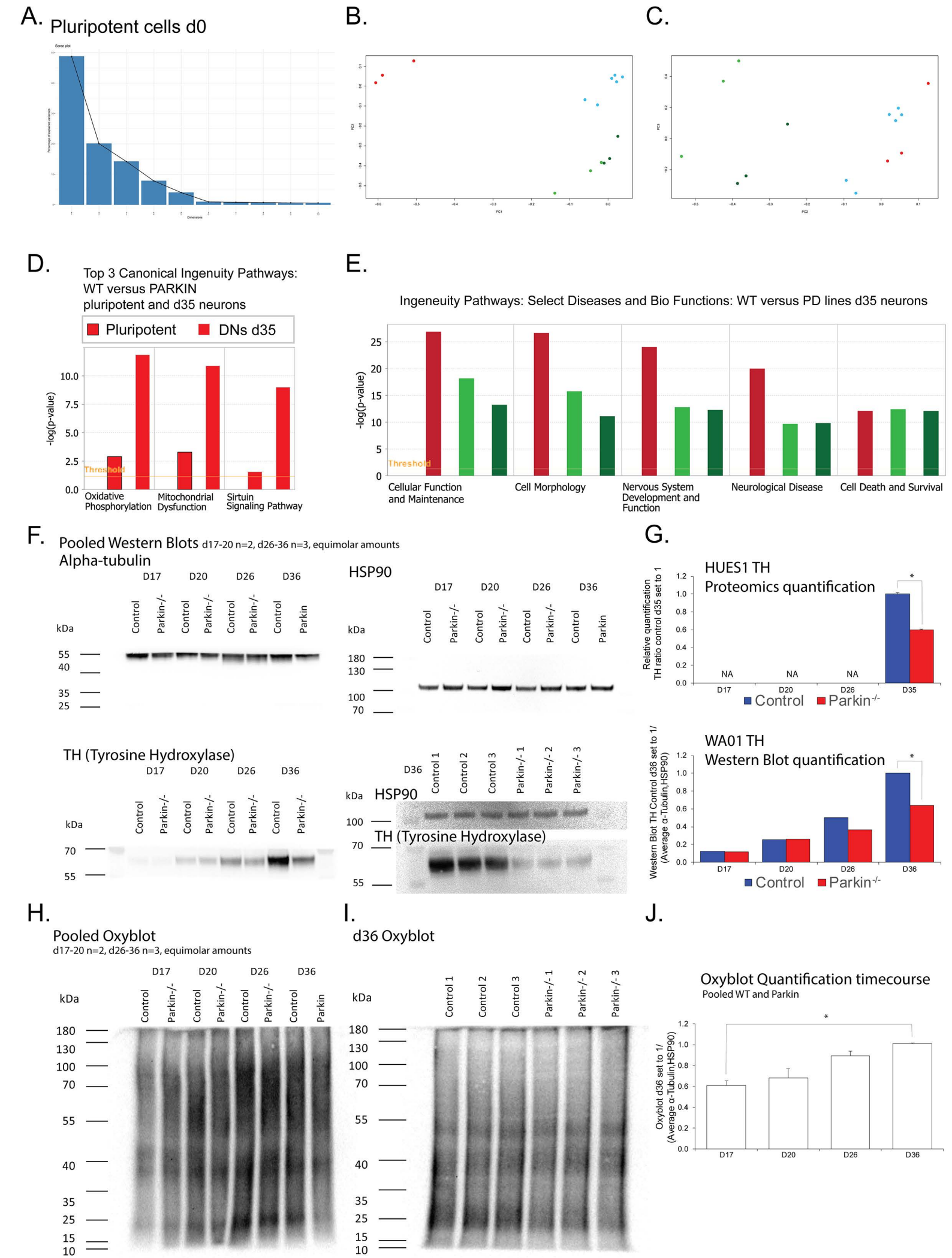

Supplemental Figure 5

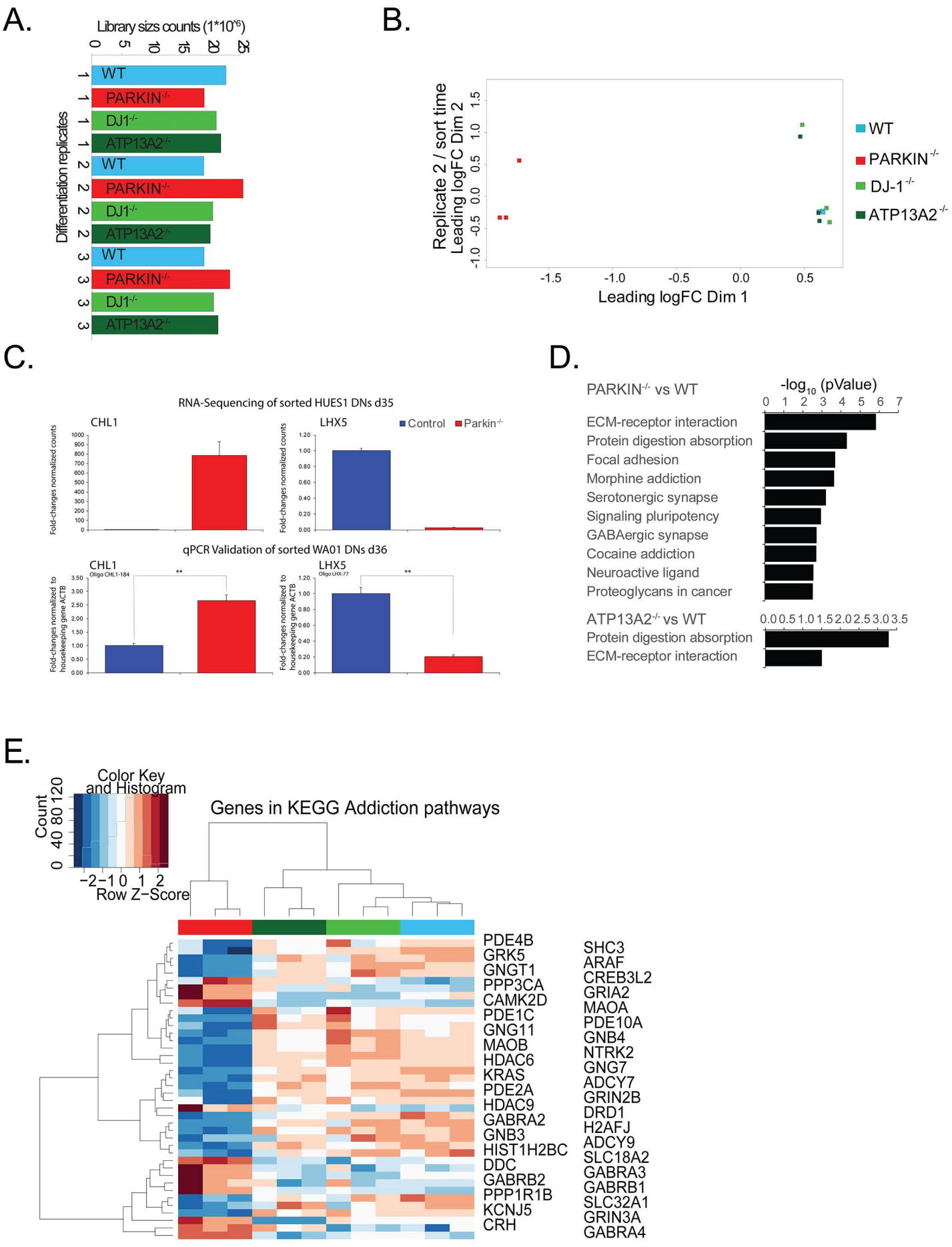

Pathogenic pathways in early onset autosomal recessive Parkinson's disease discovered using isogenic human dopaminergic neurons

Supplemental Figure 1 - Generation and Characterization of TH knock-in fluorescence reporter lines: A. Experimental scheme depicting the cloning steps taken to create basic targeting vector HR120-p2A-TdTomato as well as the additional Gibson reactions leading to the creation of the final targeting vector HR120-TH-p2A-TdTomato; B. Examples of FACS plots showing WT pluripotent control cells post nucleofection of $1*10^6$ cells with (top) vehicle control or (bottom) 5 µg CRE-GFP excision vector. A survival gate P1 was placed using FSC-A vs. SSC-A log parameters, a pulse geometry gate FSC-W vs. FSC-A was used to gate out doublets, and GFP^+ cells were sorted for clonal expansion; C. Scheme showing the PCR strategy to amplify the 5'-PCR as well as the 3'-PCR regions to confirm correctly targeted alleles; D. Potential TH-reporter knock-in clones were identified via PCR genotyping. PCR products were Sanger sequenced and aligned to the sequence expected after successful targeting; E. (left) WA01-TH WT cells were differentiated in spin culture and size was determined at d0, d15, d22, and d38, boxplots indicating size increase over time, centrality and range of spheres, (right) WA01-TH WT cells at d38 (n=3 independent differentiation experiments), boxplots indicating centrality and range of spheres; F. Fluorescence microscopy panel, showing d22 DNs dissociated on d15 and plated in low density on glial cells, from WA01-TH WT (left panel) and $PARKIN^{-/-}$ clones FB2, FB20 and FB23 (right panel). 20x Scale bar: 50 µm (left: a-TH (MAB318), middle left: a-dsRed, middle right: HOECHST, right: merge).

Supplemental Figure 2 - Derivation of isogenic cell lines: A. Examples of FACS plots showing WT pluripotent control cells post electroporation of $1*10^6$ cells with (left) vehicle control or (right) 5 µg CRISPR construct pX330 PARKIN. A survival gate P1 was placed using FSC-A vs. SSC-A parameters on log scale, a pulse geometry gate FSC-W vs. FSC-A was used to gate out doublets. mROS-G^+ cells were collected; B-D. Potential PD knockout clones were identified via PCR genotyping. PCR products were Sanger sequenced and aligned to the WT genotype; B. Potential *PARKIN* knockout clones showing exemplary mutations and proximity to guides used; C. Potential *DJ-1* knockout clones showing exemplary deletion in close proximity to the PARK7-CRISPR-1 binding site; D. Potential *ATP13A2* knockout clones showing exemplary deletion in close proximity to the PARK9-CRISPR-K binding site.

Supplemental Figure 3 - Validation of isogenic PD lines and characterization of derived DNs: A. Immunocytochemistry panel showing HUES1 isogenic reporter PD cell lines in the pluripotent state stained with TRA-1-60 (red), OCT-4 (green), and HOECHST (blue); B. Immunocytochemistry panel showing WA01-TH WT isogenic reporter cell line in the pluripotent state stained with OCT-4 (green) and HOECHST (blue); C. Karyotype analysis of WA01-TH WT, BJ-SIPS-TH WT, WA01-TH $PARKIN^{-/-}$-FB20 and $PARKIN^{-/-}$-FB23 lines; D. Dissociated spheres were analyzed via flow cytometry, examples of plots showing WA01-TH WT as well as $PARKIN^{-/-}$ lines at d22. A survival gate P1 was placed using FSC-A vs. SSC-A log parameters, a pulse geometry gate FSC-W vs. FSC-A was used to gate out doublets and TH:TdTomato number was quantified using gate P3; E. i) Live cell calcium imaging in TH^+ DNs derived from all 4 HUES1 lines by genetically encoded calcium indicator GCaMP6s. Sample fluorescence images showing GCaMP6s expression in TH^+ DNs. Scale bar: 50 µm; ii) Spontaneous calcium activities in WT DNs were blocked by incubation with sodium channel antagonist TTX (1 µM); iii) Sample intensity time plots showing spontaneous calcium activities in TH^+ DNs derived from all 4 HUES1 lines in culture medium; F. Image of full Western blot membrane corresponding to cropped images in Figure 2H. Western blot of HUES1 WT, $PARKIN^{-/-}$ and $ATP13A2^{-/-}$ lines using PARKIN antibody and GAPDH as a control at three timepoints (pluripotent state at d0, NPC at d12, and DN at d75). Mouse whole brain lysate was included as control; G. Western blot of WA01 WT and $PARKIN^{-/-}$ clones using PARKIN antibody and GAPDH as a control at d21. Mouse whole brain lysate was

used as control; H. Western blot of HUES1 WT, PARKIN$^{-/-}$, DJ-1$^{-/-}$, and ATP13A2$^{-/-}$ lines using DJ-1 antibody at three timepoints (pluripotent state at d0, NPC at d12, and DN at d75). Black arrows point to missing bands in the DJ-1$^{-/-}$ lines.

Supplemental Figure 4 - PCA of quantitative proteomics data in pluripotent cells and validation of dysregulated pathogenic pathways in HUES1-derived DNs (proteomics data): A-C. TMT proteomics results analyzed as relative abundances; A. Scree plot showing the percentage of variances explained by each principal component; B. PCA plot of components 1 and 2 at d35; C. PCA plot of components 2 and 3 at d35; D. Bar chart of d35 global proteomics comparisons between WT and all PARKIN$^{-/-}$ cell lines shows the top three dysregulated canonical ingenuity pathways using IPA curated sets. Y-axis shows the significance ($-\log_{10}$ (p-value)) and the orange line shows the significance threshold cut-off of $-\log_{10}$ (p-value = 0.05), sorted by significance in PARKIN$^{-/-}$ vs. WT comparison; E. Bar chart of d35 global proteomics comparisons between WT and all PD cell lines shows select altered disease or biological function pathways determined using IPA curated sets. Y-axis shows the significance ($-\log_{10}$ (p-value)) and the orange line shows the significance threshold cut-off of $-\log_{10}$ (p-value = 0.05), sorted by significance in PARKIN$^{-/-}$ vs. WT comparison; F. Top and bottom left: Western blot time-course analysis of WA01 WT and Parkin$^{-/-}$ samples for the housekeeping genes, alpha-tubulin and HSP90, as well as the DN marker, TH (pooled samples for display at d17 and d20 (n=2), d26 and d36 (n=3)). Bottom right: Western blot of WA01 WT and Parkin$^{-/-}$ triplicates at d36 for HSP90 and TH; G. Quantification of TH expression in pooled WA01 WT and Parkin$^{-/-}$ samples over time in comparison to d35 proteomics data from HUES1 lines, in the two genotype conditions. n=3, t-test * $p<0.05$; H. Western blot time-course analysis of pooled WA01 WT and Parkin$^{-/-}$ samples for protein carbonyl groups using the Oxyblot assay (pooled samples for display at d17 and d20 (n=2), d26 and d36 (n=3)); I. Western blot analysis of d36 WA01 WT and Parkin$^{-/-}$ triplicates for protein carbonyl groups using the Oxyblot assay; J. Quantification of protein carbonyls in pooled WA01 WT and Parkin$^{-/-}$ samples over time (n=2, t-test * $p<0.05$).

Supplemental Figure 5 - Transcriptomics Data: A. Sequencing library size in CPM (counts per million); B. Multi-dimensional scale plot of all isogenic cell lines in which distance corresponds to leading $\log_2$ fold changes between each pair of RNA samples. Dimension 1 separates the PARKIN$^{-/-}$ line from all other lines and dimension 2 separates replicate 2 from all other replicates; C. Validation of dysregulated pathogenic pathways in WA01 derived DNs (transcriptomics data). qRT-PCR analysis of sorted DNs at d36 shows dysregulation in CHL1 and LHX5 in HUES1- and WA01-derived DNs as mRNA fold change between the two genotype conditions (n=3, t-test ** $p<0.01$); D. KEGG pathway analysis showing top results for the enrichment analysis of differentially expressed transcripts in WT vs. PARKIN$^{-/-}$ and WT vs. ATP13A2$^{-/-}$ analyses (n=3); E. Heatmap across all samples using all genes associated with the KEGG term “addiction at the dopaminergic synapse.”

Supplemental Table 3 - FACS for TH percentage:

Name	Statistic	#Cells	Name	Statistic	#Cells
WT_1		50000	PARKIN_1		50000
FSC SSC	59.0	29511	FSC SSC	62.7	31347
Single Cells	95.3	28123	Single Cells	97.2	30483
TD Tomato high positive	41.3	11614	TD Tomato high positive	19.4	5914
WT_2		50000	PARKIN_2		50000
FSC SSC	63.2	31622	FSC SSC	66.6	33318
Single Cells	94.3	29823	Single Cells	96.7	32221
TD Tomato high positive	34.4	10261	TD Tomato high positive	16.8	5401
WT_3		50000	PARKIN_3		50000
FSC SSC	58.9	29474	FSC SSC	64.2	32100
Single Cells	96.3	28380	Single Cells	97.2	31190
TD Tomato high positive	30.1	8536	TD Tomato high positive	18.7	5825
WT_4		50000	PARKIN_4		50000
FSC SSC	55.5	27746	FSC SSC	62.0	30983
Single Cells	89.2	24751	Single Cells	97.1	30088
TD Tomato high positive	38.1	9429	TD Tomato high positive	16.7	5031
WT_5		50000	PARKIN_5		50000
FSC SSC	67.3	33653	FSC SSC	62.2	31102
Single Cells	91.3	30735	Single Cells	92.7	28835
TD Tomato high positive	28.2	8668	TD Tomato high positive	11.0	3184
WT_6		50000	PARKIN_6		50000
FSC SSC	66.7	33358	FSC SSC	66.3	33141
Single Cells	92.7	30937	Single Cells	94.8	31427
TD Tomato high positive	36.3	11243	TD Tomato high positive	17.4	5471
DJ-1_4		50000	ATP13A2_4		50000
FSC SSC	64.9	32458	FSC SSC	58.1	29026
Single Cells	96.3	31262	Single Cells	94.7	27495
TD Tomato high positive	29.1	9092	TD Tomato high positive	37.0	10173
DJ-1_5		50000	ATP13A2_5		50000
FSC SSC	68.4	34209	FSC SSC	66.3	33127
Single Cells	93.8	32085	Single Cells	93.7	31039
TD Tomato high positive	45.9	14726	TD Tomato high positive	47.4	14723
DJ-1_6		50000	ATP13A2_6		50000
FSC SSC	69.5	34737	FSC SSC	64.4	32218
Single Cells	93.3	32409	Single Cells	95.7	30848
TD Tomato high positive	44.7	14474	TD Tomato high positive	52.2	16092

Name	Count	Avg.	SD
WT	6	34.73333	4.922871791
P2F	6	16.66667	2.975679194
P7E	3	39.9	9.372299611
P9K	3	45.53333	7.770027885

	SS	DF
Between	2185.082778	3
Within	461.8733333	14
F	22.07759623	
P	**1.42445E-05**	****

Group 1	Group 2	Critical	P	Significant?
WT	P2F	0.008333	1.65563E-05	**Yes**
P2F	P9K	0.01	6.62576E-05	**Yes**
P2F	P7E	0.0125	0.000623274	**Yes**
WT	P9K	0.016667	0.035524519	No
WT	P7E	0.025	0.298858476	No
P7E	P9K	0.05	0.46777149	No

Supplemental Table 4 - CELLRox quantification:

Name	Count	Avg.	SD
WT TD TOMATO NEGATIVE GFP FSC SSC	4	1.355	0.50029991
WT TD TOMATO POSTIVE GFP FSC SSC	4	2.79	0.985731539
PARKIN TD TOMATO NEGATIVE GFP FSC SSC	4	6.0475	2.992349968
PARKIN TD TOMATO POSTIVE GFP FSC SSC	4	23.645	5.79446575
DJ-1 TD TOMATO NEGATIVE GFP FSC SSC	4	3.3875	2.071350204
DJ-1 TD TOMATO POSTIVE GFP FSC SSC	4	8.06	3.762516888
ATP13A2 TD TOMATO NEGATIVE GFP FSC SSC	4	4.3175	1.270206676
ATP13A2 TD TOMATO POSTIVE GFP FSC SSC	4	6.2375	1.512114965

	SS	DF
Between	1398.0047	7
Within	198.2967	24
F	24.17165274	
P	**2.09497E-09**	****

Group 1	Group 2	Critical	P	Significant?
WT TD TOMATO NEGATIVE GFP FSC SSC	PARKIN TD TOMATO POSTIVE GFP FSC SSC	0.001785714	0.000257769	**Yes**
WT TD TOMATO POSTIVE GFP FSC SSC	PARKIN TD TOMATO POSTIVE GFP FSC SSC	0.001851852	0.000393188	**Yes**
PARKIN TD TOMATO POSTIVE GFP FSC SSC	DJ-1 TD TOMATO NEGATIVE GFP FSC SSC	0.001923077	0.000589305	**Yes**
PARKIN TD TOMATO POSTIVE GFP FSC SSC	ATP13A2 TD TOMATO NEGATIVE GFP FSC SSC	0.002	0.000622833	**Yes**
WT TD TOMATO NEGATIVE GFP FSC SSC	ATP13A2 TD TOMATO POSTIVE GFP FSC SSC	0.002083333	0.00086095	**Yes**
PARKIN TD TOMATO POSTIVE GFP FSC SSC	ATP13A2 TD TOMATO POSTIVE GFP FSC SSC	0.002173913	0.001137469	**Yes**
PARKIN TD TOMATO NEGATIVE GFP FSC SSC	PARKIN TD TOMATO POSTIVE GFP FSC SSC	0.002272727	0.001668983	**Yes**
PARKIN TD TOMATO POSTIVE GFP FSC SSC	DJ-1 TD TOMATO POSTIVE GFP FSC SSC	0.002380952	0.004053602	No
WT TD TOMATO NEGATIVE GFP FSC SSC	ATP13A2 TD TOMATO NEGATIVE GFP FSC SSC	0.0025	0.004874896	No
WT TD TOMATO POSTIVE GFP FSC SSC	ATP13A2 TD TOMATO POSTIVE GFP FSC SSC	0.002631579	0.008762072	No
WT TD TOMATO NEGATIVE GFP FSC SSC	DJ-1 TD TOMATO POSTIVE GFP FSC SSC	0.002777778	0.012322761	No
WT TD TOMATO NEGATIVE GFP FSC SSC	PARKIN TD TOMATO NEGATIVE GFP FSC SSC	0.002941176	0.021295335	No
WT TD TOMATO POSTIVE GFP FSC SSC	DJ-1 TD TOMATO POSTIVE GFP FSC SSC	0.003125	0.035112571	No
WT TD TOMATO NEGATIVE GFP FSC SSC	WT TD TOMATO POSTIVE GFP FSC SSC	0.003333333	0.040865601	No
DJ-1 TD TOMATO NEGATIVE GFP FSC SSC	ATP13A2 TD TOMATO POSTIVE GFP FSC SSC	0.003571429	0.067954246	No
DJ-1 TD TOMATO NEGATIVE GFP FSC SSC	DJ-1 TD TOMATO POSTIVE GFP FSC SSC	0.003846154	0.072481277	No
WT TD TOMATO POSTIVE GFP FSC SSC	PARKIN TD TOMATO NEGATIVE GFP FSC SSC	0.004166667	0.084130695	No
ATP13A2 TD TOMATO NEGATIVE GFP FSC SSC	ATP13A2 TD TOMATO POSTIVE GFP FSC SSC	0.004545455	0.099819916	No
WT TD TOMATO NEGATIVE GFP FSC SSC	DJ-1 TD TOMATO NEGATIVE GFP FSC SSC	0.005	0.105052167	No
WT TD TOMATO POSTIVE GFP FSC SSC	ATP13A2 TD TOMATO NEGATIVE GFP FSC SSC	0.005555556	0.106157179	No
DJ-1 TD TOMATO POSTIVE GFP FSC SSC	ATP13A2 TD TOMATO NEGATIVE GFP FSC SSC	0.00625	0.108423685	No
PARKIN TD TOMATO NEGATIVE GFP FSC SSC	DJ-1 TD TOMATO NEGATIVE GFP FSC SSC	0.007142857	0.194106205	No
PARKIN TD TOMATO NEGATIVE GFP FSC SSC	ATP13A2 TD TOMATO NEGATIVE GFP FSC SSC	0.008333333	0.328113171	No
DJ-1 TD TOMATO POSTIVE GFP FSC SSC	ATP13A2 TD TOMATO POSTIVE GFP FSC SSC	0.01	0.403340847	No
PARKIN TD TOMATO NEGATIVE GFP FSC SSC	DJ-1 TD TOMATO POSTIVE GFP FSC SSC	0.0125	0.434522482	No
DJ-1 TD TOMATO NEGATIVE GFP FSC SSC	ATP13A2 TD TOMATO NEGATIVE GFP FSC SSC	0.016666667	0.473003452	No
WT TD TOMATO POSTIVE GFP FSC SSC	DJ-1 TD TOMATO NEGATIVE GFP FSC SSC	0.025	0.621068787	No
PARKIN TD TOMATO NEGATIVE GFP FSC SSC	ATP13A2 TD TOMATO POSTIVE GFP FSC SSC	0.05	0.913457289	No

Supplemental Table 1 - Proteomics Summary Table: Set 1: Intersection of d35 proteins, set 2: Intersection of pluripotent samples, all detected with confidence in two analyses that were bridged using WT-TH spheres from three independent differentiation replicates. Anova significance indicated with asterisk in column Anova, stringent pair-wise significance indicated in significance columns.

Supplemental Table 2 - Transcriptomics gene lists: Gene names as symbols, log fold changes (logFC), log counts per million (logCPM), likelihood ratio (LR), reported PValue, and false discovery rate (FDR) for all comparisons between WT and isogenic cell lines, cut-off FDR <0.01.

Supplemental Table 3 - FACS for TH percentage: Summarized table of propagated gates, FlowJo Table editor (FlowJo, LLC), FSC-A/SSC-A, and pulse geometry gate FSC-W/SSC-H. TH was quantified on a GFP-A/PE-Texas red-A gate.

Supplemental Table 4 - CellROX quantification: Summarized table of all CellROX quantification experiments, averaged mROS percentage, quantified as mROS-G^{+} using FlowJo synchronized bisector gates to divide the X-Axis into GFP^{-} and GFP^{+} non-overlapping populations based on the background expression in our unstained control (n=5, *p<0.05 ,**p<0.01). Statistical significance was analyzed by one-way ANOVA followed by Bonferroni-Holm multiple comparison test in independent staining and flow experiments, significance indicated in tables.

Supplemental Video 1 - Time-lapse video of HUES1 WT and PARKIN$^{-/-}$ cell lines between d15 and d21: Section 1. WT-Well-1 10x magnification; Section 2. WT-Well-1 representative area zoomed in; Section 3. PARKIN$^{-/-}$-Well-1 10x magnification; Section 4. PARKIN$^{-/-}$-Well-1 representative area zoomed in; Section 5. WT-Well-2 10x magnification; Section 6. WT-Well-2 representative area zoomed in; Section 7. PARKIN$^{-/-}$-Well-2 10x magnification; Section 8. PARKIN$^{-/-}$-Well-2 representative area zoomed in.

Experimental Procedures:

Dissociation of differentiated spheres

Before dissociation, HUES1 spheres were collected from spinner flasks and incubated for 1 hour in BAGTC+ 5 µM ROCK inhibitor. Spheres were transferred into falcon tubes and settled by gravity. After washing with PBS, cells were incubated for ~10 min. in 1 ml Accutase under constant manual shaking at 37°C. When spheres appeared less tight, the enzymatic digest was stopped by adding 5 ml of BAGTC+ 0.25 mg/ml DNase (Worthington Biochemical) and cells were gently triturated using a 5-ml pipette. Cells were spun at 800 RPM for 5 min. and resuspended in 1 ml BAGTC+ 5 µM ROCK inhibitor and triturated 10 times before getting filtered through a 70-µm mesh. For the WA01 cell lines, spheres were collected from spinner flasks into 12-well plates and incubated for 1 hour in BAGTC+ 10 µM ROCK inhibitor. After washing with PBS, cells were incubated for ~20 min. in 2 ml/well Accutase under constant manual shaking at RT. When spheres appeared less tight, they were gently triturated using a 5-ml pipette, followed by a 1 ml pipette tip. The dissociated spheres were transferred to 15 ml tubes containing 10 ml FACS buffer (BAGTC+ 10 uM ROCK inhibitor + 0.25 mg/ml DNase + 2% bovine calf serum (HyClone)) to stop the enzymatic digest, filtered through a 70-µm mesh and spun at 500 g for 5 min. at RT. The pellets were resuspended in 0.5 ml FACS buffer (for FACS experiments) or BAGTC+ 10 µM ROCK inhibitor (for plating) and filtered through a 0.35-µm mesh. Cells were counted using Bio-Rad cell counter and live cell dye Trypan blue. For long term culture of dissociated spheres, cells were plated on Poly-L-Lysine protein coated 96-well microplates (Greiner) coated with 1 µg/mL laminin and mouse glia (C57BL/6 Sciencell Research Laboratories #M1800-57 or CD1) at a seeding

density of 50,000 cells. For short-term imaging experiments the same plates and coatings were used, and dissociated cells were seeded at appropriate densities.

Generation of isogenic knockout lines

Human ESCs were cultured in standard conditions, and, prior to electroporation, cells were pre-treated for 1 hour with 10 μM ROCK inhibitor. $4*10^6$ cells were dissociated using Accutase (diluted at 1:3 in calcium- and magnesium-free PBS ($PBS^{-/-}$)). Cells were pelleted and resuspended in 800 μl $PBS^{-/-}$ containing 5 μg px330 CRISPR DNA or using two CRISPRs (2.5 μg each) and transferred into electroporation cuvettes. Electroporation was carried out using the Gene Pulser Xcell™ Electroporation Systems and standard settings, 250 V and 500 μF. Alternatively, nucleofection was carried out using either the P3 Nucleofector kit from Amaxa and the standard program CB-150 or the primary P4 Nucleofector kit from Amaxa and the standard program hiPSC CA137. Cells were sorted for GFP 24 hours post perturbation. GFP^+ cells were plated at clonal densities (20 cells/cm^2). Colonies were picked and expanded as clonal lines. At least 96 clones were analyzed per cell line. Genotyping PCR was used to identify clones with homozygous or compound heterozygous deletions leading to truncations and frameshift mutations. Clones for all three lines containing deletions were identified by Sanger sequencing.

Generation of the TH:TdTomato targeting vector

The final vectors were derived through modifications of the commercially available HR120-PA-1 vector (https://www.systembio.com/genome-engineering-precisionx-HR-vectors/gene-tagging). To create a new multicistronic vector, the copGFP-polyA cassette was removed using EcoRI and NruI. Vector sequence was restored via G-Block cloning which introduced a P2A cassette. The 2A self-cleaving peptide sequence is used to separate the TH protein from the TdTomato and to retain a largely unaltered endogenous TH gene product (Figure S1A). In subsequent steps the XhoI site and Gibson assembly were used to introduce the fluorophore coding sequence (CDS) followed by the Woodchuck Hepatitis virus post-translational response element (WPRE) to enhance mRNA stability and translation. For example, the TdTomato CDS followed by the WPRE element was amplified using pFUGW-TdTomato as a template. The PCR product was inserted via Gibson cloning. To add 5' homology arms to the HR120-p2A-TD-TOM, the vector has to be cut with the restriction endonuclease NheI. A homology arm is created either by PCR or DNA synthesis utilizing 18-40 bp long overlap sequences between the vector and insert. A template for the DNA generation is given below. Vector and homology arm are enzymatically assembled using Gibson reaction. In a subsequent step, BamHI restriction endonuclease can linearize the vector to add a 3' homology arm. The 5' homology arm ends before the stop codon of the gene of interest to allow for a fusion protein or multicistronic expression. The necessary overhangs are shown in detail in Table 1. In the case of the TH targeting vector (TH-HR120-TdTomato-WPRE), we used ~500-bp sequences with homology to the targeted *TH* locus that can act as homology arms. After the removal of the stop codon, the last exon of the *TH* gene is fused to an in-frame p2A-TdTomato sequence followed by the WPRE site and a loxP-flanked drug-resistance cassette (Figure S1A).

Table 1 - Nucleotide sequence that can be used to create overlapping sequence for Gibson assembly

HR120-p2A-TdTomato:	NheI and BamHI
GACGTTGTAAAACGACGGCCAGTGAATTCAGCTAG	5 Prime 1st overhang (NheI digest)

GCTAGCGGAAGCGGAGCTACTAACTTCAGCCTGTTGA	5 Prime 2nd overhang (NheI digest)
CACGTAAGTAGAACATGAAATAACCTAGATCGGATC	3 Prime 1st overhang (BamHI digest)
GATCCCCGTCGACTGCATGCAAGCTTGGCGTAATC	3 Prime 2nd overhang (BamHI digest)

Generation of TH-reporter knock-in lines

Nucleofection was carried out using either the P3 Nucleofector kit from Amaxa and the standard program CB-150 or the primary P4 Nucleofector kit from Amaxa and the standard program hiPSC CA137. Best nucleofection conditions were different using two Amaxa 4D-Nucleofector™ X units. 1-2*10^6 cells were dissociated using Accutase (diluted at 1:3 in $PBS^{-/-}$). Cells were pelleted and resuspended in 100 µl nucleofection solution loaded with two different CRISPR constructs (2 µg px330 CRISPR DNA each) plus 5 µg targeting vector and transferred into electroporation cuvettes. To improve the odds of successful targeting, we created CRISPR/Cas9 constructs by cloning CRISPR guide sequences into the pX330 Cas9 plasmid (Cong et al., 2013). We selected CRISPR guide sequences that were located on opposite strands overlapping with the stop codon of the *TH* gene. Guides were designed to exhibit overlapping sequences in both homology arms to prevent binding of the CRISPR to the targeting vector. Cells were recovered in mTESR on plates pre-coated with Matrigel. After nucleofection of hPSCs with both TH-CRISPR-Cas9 expression vectors as well as the pHR120-TH:TdTomato-WPRE plasmid (Figure S1A), they were cultured in the presence of Puromycin for 2 days. We then observed the emergence of Puromycin-resistant clones that maintained hPSC-like morphology. Cells were allowed to grow to confluency. To excise the selection cassette, we nucleofected mixed clones containing 100 to 200 selected colonies with pCAG-Cre:GFP (Matsuda and Cepko, 2007). To enrich for cells that received the CRE plasmid, we enriched for GFP^+ cells using flow sorting (Figure S1B). We expanded 24 clonal cell lines. Post Cre excision we screened for homologous recombination and correct gene insertion using primers outside the targeting arm and inside the targeting vector (Figure S1C). The 5'-PCR yielded a strong PCR band of 626 bp size while the 3'-PCR showed the expected band size at 878 bp. We used Sanger sequencing to analyze the resulting PCR products (Figure S1D).

Electrophysiology and calcium imaging

As previously described (Eden et al., 2009; Rigamonti et al., 2016), whole-cell patch clamp recordings were performed with a Multiclamp 700B amplifier and a Digidata 1550 Digitizer (Molecular Devices). Data were collected using pClamp 10 software (Molecular Devices), sampled at 10 kHz, and filtered at 1 kHz. Cells were continually perfused with Tyrode's solution at RT: 128 mM NaCl, 30 mM glucose, 25 mM HEPES, 5 mM KCl, 2 mM $CaCl_2$, and 1 mM $MgCl_2$ (adjusted to pH 7.3 with NaOH). Patch pipettes were pulled from borosilicate glass using a P-1000 Micropipette Puller (Sutter Instrument) with resistance of 4-8 MΩ when filled with pipette solution containing: 147 mM KCl, 5 mM Na_2-phosphocreatine, 2 mM EGTA, 10 mM HEPES, 2 mM MgATP, and 0.3 mM Na_2GTP (adjusted to pH 7.3 with KOH). For voltage-clamp recordings, membrane potential was held at -70 mV. For current-clamp recordings, resting membrane potential was adjusted to -60 mV by a small current injection. For sodium/potassium current recordings, membrane potential was depolarized from -60 mV to 50 mV in 10 mV increments.

Live cell calcium imaging

DNs were seeded on top of CD1 mouse cortical astrocytes after flow sorting and infected with AAV1-Syn-GCaMP6s (Penn Vector Core, #AV-1-PV2824). Live cell imaging with perfusion was performed on a Nikon Eclipse Ti-S Inverted microscope with a perfusion chamber. Cells were continuously perfused with Tyrode's solution at RT. Time-lapse recordings were acquired at 1 frame per second with a 20x objective. Mean fluorescent intensity of GCaMP6s was measured in cell soma by ImageJ (U.S. National Institutes of Health, http://imagej.nih.gov/ij/), normalized to the minimal intensity, and plotted by Igor (WaveMetrics).

Flow analysis and FACS of midbrain DNs

To assess the percentage and create pure cultures of TH^+ cells, spheres were analyzed using a BD LSR-II analyzer and sorted using a BD FACSAria II flow sorter. Cells were dissociated and counted and medium adjusted to contain no more than 2 million cells per ml and transferred into Falcon® 5-mL round-bottom Polystyrene test tubes, with cell strainer snap caps and run on the 15-parameter BD FACSAria II+, customized for small particle to average cell (<0.1 microns) sorting using a low-pressure nozzle and custom settings. Forward scatter (FSC) and side scatter (SSC) were used to eliminate debris in conjunction with FSC-width (FSC-W) and SSC-area (SSC-A) to focus on single cells. TdTomato fluorescence vs. GFP fluorescence was used to select TH^+ cells and remove dead cells (auto-fluorescence in the green channel). Data was analyzed using FlowJo or FCS express software. Dissociation of tight neurospheres is a critical step as the process will inevitably lead to cell death and debris. Debris and dead cells typically have a lower level of FSC-A and SSC-A which are found in the lower left part of the scatter plot (Figure S2A, left panel). We gated to exclude most dead cells and debris. We used a pulse geometry gate FSC-W and SSC-height (SSC-H) to gate out doublets (Figure S2A, middle panel). We quantified TH expression on a GFP-A PE-Texas red-A gate against a negative pluripotent control (Figure S2A, right panel and Table S3). Usually, we performed experiments in triplicates. Some experiments were quantified using more differentiation replicates. We repeated the quantification of TH^+ neurons at d35 in 6 (WT and $PARKIN^{-/-}$ lines) and 3 ($DJ\text{-}1^{-/-}$ and $ATP13A2^{-/-}$ lines) independent differentiations. To measure CellROX positivity, we performed a total of 4 differentiation experiments for each line and stained independently twice. CellROX exhibits green fluorescence upon oxidation by mROS with an absorption/emission maximum of ~485/520 nm. In a histogram, we overlaid results from the unstained control, the WT line and the $PARKIN^{-/-}$ line (Figure 3E). In our flow cytometry analysis of the cells, we gated on TH^+ and TH^- cells and measured GFP intensity (Table S4).

Nikon BioStation CT imaging

For live cell imaging in the Nikon BioStation CT, we dissociated all isogenic lines at d15. We determined live cell numbers using an automated cell counter and Trypan blue staining and plated $5x10^4$ unsorted live cells per well for each cell line into a 96-well plate pre-coated with mouse glia at a seeding density of 50,000 cells. In previous experiments, we found almost uniform expression of the NPC marker NESTIN in our cultures at this time, with approximately 5% of the cells expressing TdTomato. We began image acquisition at d16, 24 hours post dissociation. Images were acquired every 6 hours over 8 days until d25 of differentiation.

Immunocytochemistry

Cells were fixed with either 5% PFA or cold methanol (-80°C) as indicated in Table 2. Cells were blocked in 0.1% Triton X-100 (Sigma) in 5% horse serum/PBS, and then incubated in primary antibody (0.1% Triton X-100 in 5% horse serum/PBS) overnight at 4°C. On the following day, cells

were washed in PBS-T, incubated in species-specific fluorophore conjugated Alexa fluor secondary antibodies and HOECHST nuclear stain according to the manufacturer's protocol.

Table 2 – Antibodies used for immunocytochemistry experiments.

Company	Target	Antibody
Abcam	TRA-1-60	ab16288
Abcam	OCT4	ab19857
Abcam	FOXA2	ab60721
Abcam	LMX1A	ab139726
Pel Freez	TH	P40101-0
Millipore	TH	MAB318
VWR	RFP	RL600-401-379

IHC and image analysis of sectioned spheres:

Serial sections (4-6 µm) of paraffin-preserved midbrain organoid sections were prepared using a Leica RM2255 microtome and used for IHC analysis. Organoids from the WA01-TH WT cell line were fixed with 4% PFA for 5 min. and embedded on d0, d15, d22, and d38 of differentiation. Sections were placed on charged slides and baked overnight at 70°C. IHC was performed on Ventana Benchmark XT. Antigen retrieval with CC1 (citric acid buffer) was performed for 1 hour followed by primary antibody incubation for 30 min. The primary antibodies used are listed in Table 3. A multimer secondary antibody was used for all samples. IHC sections were imaged using a Nikon Eclipse Ci-L equipped with a Nikon Digital Sight DS-Fi2 camera. Live d22 spheres from the BJ-SIPS-TH WT cell line were imaged using spinning disc confocal CX7. Maximum projections were generated using z-stack images that were acquired in laser confocal mode in 10x magnification, pin hole size 70.

Table 3 – Antibodies used for IHC experiments.

Company	Target	Antibody
Thermo Fisher Scientific	TRA-1-60	41-1000
Cell Signaling Technology	OCT4	2750
Abcam	FOXA2	ab60721

Sigma	LMX1A	HPA030088
Pelfreeze	TH	P40101-150
Millipore	TH	MAB318
Rockland	RFP	600-401-379

Karyotype analysis

We utilized Giemsa stained mitotic chromosome preparation (G-banding) to screen for genomic abnormalities (>5-10 Mb), inversion, duplications, deletions, translocations or aneuploidies in WT-TH cell lines and select clones. The analysis was performed by the WiCell cytogenetics laboratory with protocols optimized for hPSCs. Twenty metaphase spreads were analyzed for each sample. Karyotypic abnormalities are frequently discovered after genome editing and selection in hPSCs. We made large freezes of cells prior to karyotyping and routinely return to low passage stocks to avoid working with cells that may acquire chromosomal changes post analysis. WA01-TH and BJ-SIPS-TH cell lines and selected clones were normal as indicated. Karyotype analysis in the original HUES1-TH WT donor cell line revealed an extra copy of the short-arm of chromosome 12 from band p13.33 to p11.1 and loss of the short-arm of chromosome 10 from band p14 to p12.2 typical for survival and growth advantage of pluripotent stem cells. The abnormalities were propagated in isogenic descendants.

RNA extraction

WA01 derived DNs were sorted on d36 for RNA extraction using the Monarch Total RNA Miniprep Kit (NEB). The SuperScript IV First-Strand Synthesis System (Invitrogen) was then used to prepare the cDNA samples.

qRT-PCR

The qRT-PCR mixes were loaded with SYBR Green PCR Master Mix (Applied Biosystems) for analysis using the QuantStudio System (Applied Biosystems). qRT-PCR primers were designed to be exon spanning (Table 4). We chose highly dysregulated genes that were identified in the transcriptomics studies of HUES1 WT and Parkin$^{-/-}$ cell lines. Here, we differentiated WA01 WT and Parkin$^{-/-}$ cells in three independent experiments. We then sorted the DNs at d36 and performed qRT-PCR. We tested CHL1 and LHX5 expression that showed strong dysregulation between WT and Parkin$^{-/-}$ lines and could successfully be amplified via qRT-PCR (Figure S5C). Both recapitulated the expected dysregulation in the same direction. CHL1 likely plays a role in cell adhesion and synaptic function and has not been investigated in the context of Parkin dysregulation but has been discussed as a risk gene for Parkinsonism (Pottier et al., 2018). We interpreted the presence of LHX5 as incomplete midbrain patterning. Cells that receive too little WNT signaling show hypothalamic LHX5 expression in our system. It is unclear whether the reduced transcript abundance in the Parkin$^{-/-}$ line represents a type of survival or differentiation bias, but the data are consistent across cell lines.

Table 4 - The primer sequences used for qRT-PCR analysis.

LHX5	Forward primer	GTTCGTGTGCAAAGACGACTAC
	Reverse primer	CCGTACAGGATGACACTGAGTT
CHL1	Forward primer	TGGCATCTTGTTATGTGAGGCT
	Reverse primer	TCCATGGACATTTGAGGCTTCA
ACTB	Forward primer	ACCGGGCATAGTGGTTGGA
	Reverse primer	ATGGTACACGGTTCTCAACATC

Western blotting

Cell culture lysates were generated using RIPA Lysis and Extraction Buffer (Thermo Fisher Scientific), or 2% SDS lysis buffer (50 mM tris, 100% glycerol, and 10% SDS) containing protease inhibitor cocktail (100x; Roche) and phosphatase inhibitor cocktail (100x; Abcam), or 18% SDS lysis buffer (1 M tris-HCl (pH 6.8), 8 M urea, 20% glycerol, and 18% SDS). Protein concentration was estimated using the Pierce BCA Protein Assay Kit (Thermo Fisher Scientific). For Western blot analysis 20-40 µg total protein was denatured under reducing conditions in 4x Laemmli Sample Buffer (Bio-Rad) by boiling in 4X Bolt LDS Sample Buffer (Novex) for 10 min. at 98°C prior to loading onto a 10% Criterion TGX Precast gel (Bio-Rad) or a NuPAGE 4-12% Bis-Tris Gel (Invitrogen), then transferred to a PVDF or nitrocellulose membrane (0.22 µm; Bio-Rad or Novex) using the Criterion Blotter system (Bio-Rad) or iBlot 2 dry blotting system (Invitrogen). Membranes were blocked for 1 hour at RT in 5% w/v non-fat milk (Santa Cruz) or BSA (Sigma) in TBS containing 0.1% v/v Tween-20 (Fisher Scientific; TBS-T). Membranes were then incubated in the indicated primary antibody (in 5% milk or BSA/TBS-T) overnight at 4°C, washed 4 times in TBS-T, incubated in species-specific HRP-conjugated secondary antibody (in 5% milk or BSA/TBS-T) for 1 hour at RT, and then washed 4 times in TBS-T. Membranes were subsequently developed with ECL Western blotting substrate (Pierce or PerkinElmer) and immunodetection was performed using the ChemiDox XRS$^+$ System (Bio-Rad). Membranes were then washed once in TBS-T and stripped in stripping buffer (25 mM Glycine HCl, pH 2.0 and 1% w/v SDS) with vigorous shaking to remove primary and secondary antibodies, washed three times in TBS-T, and blocked for 1 hour (in 5% milk/TBS-T) at RT before probing with the next primary antibody. The antibodies used are listed in Table 5.

Table 5 – Antibodies used for Western blots experiments.

Company	Target	Antibody
Santa Cruz	PARKIN PRK8	sc-32282
Abclonal	DJ-1 PARK7	A0987
Thermo Fisher Scientific	GAPDH	4300
Cell Signaling Technology	HSP90	4874

Semi-quantitative Western blot to determine TH expression

Samples of midbrain DN spheres were collected at specific timepoints for protein extraction, quantification, and Western blot analysis as described above. The results were quantified using Image Studio Lite (LI-COR Biosciences). To validate that TdTomato expression is reflective of TH expression and to confirm the quantified reduced TH expression in quantitative proteomics experiments, we employed Western blot techniques using the developmental timepoints d17, d20, d26, and d36 in three independent differentiation experiments of WA01 WT and Parkin$^{-/-}$ lines. We pooled differentiation experiments for display of developmental timepoints using equimolar inputs. We first tested several housekeeping genes in a time-course. Alpha-tubulin and HSP90 show consistent expression across samples and timepoints (Figure S4F, top panel). We used an average of these housekeeping genes for all normalizations and quantifications. In line with our flow cytometry findings, TH expression increased over time during terminal differentiation (Figure S4F, bottom left panel). HPS90 and TH expression is also shown for individual samples at d36 (Figure S4F, bottom right). Experiments in the HUES1 cell line showed that TH protein abundance is about 50% lower in Parkin$^{-/-}$ cells using iTRAQ relative quantification of protein abundance (Figure S4G, top panel). Here we confirm the significantly reduced TH protein expression at d35 in independent WA01 derived Parkin$^{-/-}$ cells (Figure S4G, bottom panel).

Table 6 - The primary and secondary antibodies used for semi-quantitative Western blot analysis.

Primary antibody	Company	Catalog Number	Dilution
Alpha-tubulin	Sigma-Aldrich	T6074	1:4000
HSP90	Cell Signaling	4874S	1:10,000
Tyrosine hydroxylase	Millipore	MAB318	1:1000
Secondary antibody			
Anti-mouse	Jackson IR	715-035-150	1:10,000
Anti-rabbit	Jackson IR	711-035-152	1:10,000

Oxyblot assay

Protein carbonyl groups of individual or pooled whole lysates were derivatized with DNP using the OxyBlot Protein Oxidation Detection Kit (EMD-Millipore) reagents and conditions according to the manufacturer. To validate that OS is connected to DN physiology, we utilized the Oxyblot techniques in a time-course experiment as well as on d36 (Figures S4H-I). Oxyblots measure protein carbonyl content, which is considered a marker of oxidative modification of proteins and, therefore, of OS (Butterfield et al., 2010). In a series of experiments using this method, we found that the quantity of carbonylated proteins in differentiating hPSCs increased over time and was significantly different between d17 and d35 (Figure S4J). We believe that this observation reflects the unique properties of DNs and their well-known oxidation of dopamine in response to OS (Burbulla et al., 2017; Surmeier et al., 2017). However, we did not observe a significant increase of protein carbonylation in Parkin$^{-/-}$ midbrain spheres compared to WT controls. At the time of the experiments, WA01 Parkin$^{-/-}$ spheres contain fewer than half the number of TH^{+} DNs. Thus, we hypothesize that the Parkin$^{-/-}$ DNs likely experienced more OS per neuron, but that was balanced by a reduced number of DNs in the spheres. Future experiments using sorted DNs or inhibition of TH during the differentiation might increase our understanding of this mechanism.

mRNA-Seq library preparation and sequencing

RNA extraction for mRNA sequencing was performed post flow sorting of at least 200,000 TH^+ cells using Qiagen micro RNA extraction with on-column DNase digest. RNA amount and integrity were approximated using the bioanalyzer 2100 RNA Nano kit. Illumina mRNA-seq libraries were prepared using the TruSeq RNA kit using 200 ng of total RNA per sample. Library sequencing was carried out on a HiSeq2500 in rapid mode, 1 lane/pool. Each pool contained 6 samples, 3 differentiation replicates per isogenic cell line. The concentration of both pools was approximately 2.6 ng/µl and each library was sequenced to a depth of ~60 million fragments using 50 bp paired-end reads. RNA-seq reads were mapped using TopHat version 2.0.9 against the human genome build GRCh38. The primary assembly was downloaded from primary assembly from ftp://ftp.ensembl.org/pub/release-85/fasta/homo_sapiens/dna/.

Gene expression analysis

FASTQ files were aligned to the primary assembly ENSEMBL GRCh38 index built ftp://ftp.ensembl.org/pub/release-85/fasta/homo_sapiens/dna/ using Tophat. For annotations, we used a GTF transcriptome build GRCh38 here: ftp://ftp.ensembl.org/pub/release-85/gtf/homo_sapiens. Gene expression analysis was carried out with the statistical software R and several Bioconductor packages including edgeR (McCarthy et al., 2012; Robinson et al., 2010). Data was normalized using standard edgeR parameters. We excluded low count genes (less than 30 counts in at least 2 conditions). Using the generalized linear modeling framework of edgeR, we identified DEGs between all experimental conditions. Multiplicity correction applying the Benjamini-Hochberg method was performed on the p-values, to control the FDR (false discovery rate). Table S2 contains original countable and pairwise comparisons between WT and isogenic PD lines. Log-fold changes and FDRs.

Proteomics - Cell lysis and protein digestion

Cells were lysed in 8 M urea and 50 mM EPPS with sonication. The homogenate was sedimented by centrifugation at 21,000 x g for 5 min. Proteins were subjected to disulfide bond reduction with 5 mM tris(2-carboxyethyl)phosphine (RT, 30 min.) and alkylation with 10 mM chloroacetamide (RT, 30 min. in the dark). Methanol-chloroform precipitation was performed prior to protease digestion. Samples were resuspended in 200 mM EPPS (pH 8.5) and digested at RT for 13 hours with LysC protease at a 100:1 protein-to-protease ratio. Trypsin was then added at a 100:1 protein-to-protease ratio and the reaction was incubated for 6 hours at 37°C.

AQUA proteomics

For AQUA/PRM, samples were subjected to Trichloroacetic acid (TCA) precipitation. Samples were first digested with Lys-C (in 100 mM tetraethylammonium bromide (TEAB), 0.1% Rapigest (Waters Corporation), 10% (vol/vol) acetonitrile (ACN)) for 2 hours at 37°C, followed by the addition of trypsin and further digested for 6 hours at 37°C. Digests were acidified with an equal volume of 5% (vol/vol) formic acid (FA) to a pH of ~2 for 30 min., dried down, and resuspended in 1% (vol/vol) FA.

For PARKIN AQUA/PRM, three heavy-labeled reference peptides (QGVPADQL**R**; ILGEEQYN**R**; VCMGDHW**F**DV – where Cysteine is carboxyamidometylated and Methionine oxidized), each containing a single 13C/15N-labeled amino acid (indicated in bold and underlined), was produced at Cell Signaling Technologies and quantified by amino acid analysis. AQUA peptides from working stocks (in 5% (vol/vol) FA) were diluted into the digested sample (in 1% (vol/vol) FA) to be analyzed to an optimal final concentration predetermined for individual peptides. Samples and AQUA peptides were oxidized with 0.05% hydrogen peroxide for 20 min. at RT, subjected to C18 StageTip, and resuspended in 1% (vol/vol) FA. MS data were collected sequentially by LC/MS on an Orbitrap Fusion Lumos mass spectrometer (Thermo Fisher Scientific) coupled to a Proxeon EASY-nLC 1200 liquid chromatography (LC) pump (Thermo Fisher Scientific). The capillary

column was a 100 µm inner diameter microcapillary column packed with ~35 cm of Accucore resin (2.6 µm, 150 Å, Sepax). For each analysis, ~2 µg was loaded onto the column. The samples were analyzed by targeted Single Ion Monitoring (t-SIM), with the peptides of interest (heavy and light) defined in an inclusion list by their m/z and charge. The scan sequence began with an Orbitrap MS1 SIM scan for the targeted peptides with an isolation window of 1.7 m/z with the following parameters: resolution of 120,000, AGC target of 1×10^5, maximum injection time of 200 ms, and multiplexing option (MSX) was set to 2 and defined as the pair of heavy and light peptides to be analyzed. This scan was followed by 2 targeted MS2 scans selected from the inclusion list. Each targeted MS2 scan consisted of high-energy collision dissociation (HCD) with the following parameters: resolution of 30,000, AGC of 5×10^4, maximum injection time of 200 ms, isolation window of 1.6 m/z, and normalized collision energy (NCE) of 30. Raw files were imported, and precursor and fragment ions were quantified using Skyline version 3.5. Data generated from Skyline were exported into Excel and PRISM for further analysis. Total PARKIN abundance was determined as the average of the abundance calculated for each individual peptide.

Proteomics - Tandem mass tag labeling

Multiplexing in TMT-based approaches is limited by the number of isobaric tags. To allow comparative studies, we used WT differentiation replicates as bridge channels. Briefly, 50 µg peptides, resuspended in 100 µl of 0.1 M EPPS (pH 8.5) from each sample were labeled with TMT reagent. A total of 5 µL of the 20 ng/µL stock of TMT reagent was added to the peptides along with 25 µL of acetonitrile to achieve a final acetonitrile concentration of approximately 20% (v/v). Following incubation at RT for 1 hour, the reaction was quenched with hydroxylamine to a final concentration of 0.5% (v/v) for 15 min. The TMT-labeled samples were pooled together at a 1:1 ratio. The sample was vacuum centrifuged to near dryness and subjected to C18 solid-phase extraction (SPE) (Sep-Pak, Waters).

Proteomics - Off-line basic pH reversed-phase (BPRP) fractionation

We fractionated the pooled TMT-labeled peptide samples using BPRP HPLC (Wang et al., 2011). We used an Agilent 1100 pump equipped with a degasser and a photodiode array (PDA) detector (set at 220 and 280 nm wavelengths; Thermo Fisher Scientific). Peptides were subjected to a 50-min. linear gradient from 5% to 35% acetonitrile in 10 mM ammonium bicarbonate (pH 8) at a flow rate of 0.8 mL/min. over an Agilent 300Extend C18 column (5 µm particles, 4.6 mm ID and 220 mm in length). The peptide mixture was fractionated into a total of 96 fractions, and concatenated non-consecutively for a total of 12 fractions. Samples were subsequently acidified with 1% formic acid and vacuum centrifuged to near dryness. Each consolidated fraction was desalted via StageTip, dried again via vacuum centrifugation, and reconstituted in 5% acetonitrile, 5% formic acid for LC-MS/MS processing.

Proteomics - Liquid chromatography and tandem mass spectrometry

Mass spectrometry data were collected using an Orbitrap Fusion Lumos mass spectrometer (Thermo Fisher Scientific) coupled to a Proxeon EASY-nLC 1000/1200 liquid chromatography (LC) pump (Thermo Fisher Scientific). The capillary column was a 100 µm inner diameter microcapillary column packed with ~35 cm of Accucore resin (2.6 µm, 150 Å, Sepax). For each analysis, we loaded ~2 µg onto the column.

Each peptide fraction was separated using a 2.5 h gradient of 6 to 26% acetonitrile in 0.125% formic acid at a flow rate of ~450 nL/min. Each analysis used the Multi-Notch MS3-based TMT method (McAlister et al., 2014), a method that reduces ion interference compared to MS2 quantification (Paulo et al., 2016). The scan sequence began with an MS1 spectrum (Orbitrap analysis; resolution 120,000; mass range 400−1400 m/z; automatic gain control (AGC) target 2×10^5; maximum injection time 100 ms). Precursors for MS2 analysis were selected using a

Top10 method. MS2 analysis consisted of collision-induced dissociation (quadrupole ion trap analysis; AGC 4×10^3; normalized collision energy (NCE) 35; maximum injection time 150 ms). Following acquisition of each MS2 spectrum, a synchronous-precursor-selection (SPS) MS3 scan was collected on the top 10 most intense ions in the MS2 spectrum (McAlister et al., 2014). MS3 precursors were fragmented by high energy collision-induced dissociation (HCD) and analyzed using the Orbitrap (NCE 55; AGC 5×10^4; maximum injection time 150 ms, resolution was 60,000 at 200 Th).

Proteomics - Data analysis

Mass spectra were processed using Proteome Discoverer (v2.3.0.420 - Thermo Fisher Scientific). The identification of proteins was performed using the SEQUEST-HT engine against the UniProt Human Reference Proteome (2018 - SwissProt and TrEMBL) using the following parameters (post-recalibration): a tolerance level of 15 ppm for MS^1 and 0.6 Da for MS^2 and false discovery rate of the Percolator decoy database search was set to 1%. Trypsin and LysC were used as the digestion enzyme, two missed cleavages were allowed, and the minimal peptide length was set to 7 amino acids. TMT tags on lysine residues and peptide N termini (+229.163 Da) and carbamidomethylation of cysteine residues (+57.021 Da) were set as static modifications, while oxidation of methionine residues (+15.995 Da) was set as a variable modification. For TMT-based reporter ion quantitation, we extracted (integration tolerance of 0.003 Da) the summed signal-to-noise ratio for each TMT channel and found the closest matching centroid to the expected mass of the TMT reporter ion. For protein-level comparisons, PSMs were identified, quantified, and collapsed to a 1% peptide FDR and then collapsed further to a final protein-level FDR of 1%. Moreover, protein assembly was guided by principles of parsimony to produce the smallest set of proteins necessary to account for all observed peptides. Proteins were quantified by summing reporter ion counts across all matching PSMs unique and razor peptides. PSMs with poor quality, MS^3 spectra with TMT reporter summed signal-to-noise ratio that were less than 10 per channel, isolation specificity ≤0.4, or had less than 70% of correctly selected SPS ions were excluded from quantification (McAlister et al., 2012).

Protein quantification values were exported for further analysis in Microsoft Excel and Perseus (Tyanova et al., 2016). Each reporter ion channel was summed across all quantified proteins and normalized assuming equal protein loading of all 10 samples. Table S1 lists all quantified proteins as well as associated TMT reporter fold change to control channels (WT cells) used for quantitative analysis.

IPA Analysis

The proteomics and transcriptomics datasets included NCBI gene symbols as identifiers, log2 ratios and p-values for each gene. This information was input for IPA using the core analysis platform (Ingenuity Systems). Core analysis settings fold change cut-offs were different for each of our datasets using the following log2 ratios: proteomics pluripotent d0, proteomics DN d35 and transcriptomics DN d35. This was to ensure that the number of enriched or underrepresented proteins/transcripts fell into a similar range and allowed statistically meaningful analysis. IPA generated lists of enriched molecular networks, canonical pathways and biological functions that included disease pathways and that were used to probe dysregulation of pathways previously implicated in PD etiology.

Citations:

Burbulla, L.F., Song, P., Mazzulli, J.R., Zampese, E., Wong, Y.C., Jeon, S., Santos, D.P., Blanz, J., Obermaier, C.D., Strojny, C.*, et al.* (2017). Dopamine oxidation mediates mitochondrial and lysosomal dysfunction in Parkinson's disease. Science *357*, 1255-1261.
Butterfield, D.A., Galvan, V., Lange, M.B., Tang, H., Sowell, R.A., Spilman, P., Fombonne, J., Gorostiza, O., Zhang, J., Sultana, R.*, et al.* (2010). In vivo oxidative stress in brain of Alzheimer disease transgenic mice: Requirement for methionine 35 in amyloid beta-peptide of APP. Free Radic Biol Med *48*, 136-144.
Eden, E., Navon, R., Steinfeld, I., Lipson, D., and Yakhini, Z. (2009). GOrilla: a tool for discovery and visualization of enriched GO terms in ranked gene lists. BMC bioinformatics *10*, 48.
Matsuda, T., and Cepko, C.L. (2007). Controlled expression of transgenes introduced by in vivo electroporation. Proc Natl Acad Sci U S A *104*, 1027-1032.
McAlister, G.C., Huttlin, E.L., Haas, W., Ting, L., Jedrychowski, M.P., Rogers, J.C., Kuhn, K., Pike, I., Grothe, R.A., Blethrow, J.D.*, et al.* (2012). Increasing the multiplexing capacity of TMTs using reporter ion isotopologues with isobaric masses. Analytical chemistry *84*, 7469-7478.
McAlister, G.C., Nusinow, D.P., Jedrychowski, M.P., Wuhr, M., Huttlin, E.L., Erickson, B.K., Rad, R., Haas, W., and Gygi, S.P. (2014). MultiNotch MS3 enables accurate, sensitive, and multiplexed detection of differential expression across cancer cell line proteomes. Analytical chemistry *86*, 7150-7158.
McCarthy, D.J., Chen, Y., and Smyth, G.K. (2012). Differential expression analysis of multifactor RNA-Seq experiments with respect to biological variation. Nucleic Acids Res *40*, 4288-4297.
Paulo, J.A., O'Connell, J.D., and Gygi, S.P. (2016). A Triple Knockout (TKO) Proteomics Standard for Diagnosing Ion Interference in Isobaric Labeling Experiments. Journal of the American Society for Mass Spectrometry *27*, 1620-1625.
Pottier, C., Zhou, X., Perkerson, R.B., 3rd, Baker, M., Jenkins, G.D., Serie, D.J., Ghidoni, R., Benussi, L., Binetti, G., Lopez de Munain, A.*, et al.* (2018). Potential genetic modifiers of disease risk and age at onset in patients with frontotemporal lobar degeneration and GRN mutations: a genome-wide association study. Lancet Neurol *17*, 548-558.
Rigamonti, A., Repetti, G.G., Sun, C., Price, F.D., Reny, D.C., Rapino, F., Weisinger, K., Benkler, C., Peterson, Q.P., Davidow, L.S.*, et al.* (2016). Large-Scale Production of Mature Neurons from Human Pluripotent Stem Cells in a Three-Dimensional Suspension Culture System. Stem cell reports *6*, 993-1008.
Robinson, M.D., McCarthy, D.J., and Smyth, G.K. (2010). edgeR: a Bioconductor package for differential expression analysis of digital gene expression data. Bioinformatics *26*, 139-140.
Surmeier, D.J., Obeso, J.A., and Halliday, G.M. (2017). Selective neuronal vulnerability in Parkinson disease. Nat Rev Neurosci *18*, 101-113.
Tyanova, S., Temu, T., Sinitcyn, P., Carlson, A., Hein, M.Y., Geiger, T., Mann, M., and Cox, J. (2016). The Perseus computational platform for comprehensive analysis of (prote)omics data. Nat Methods *13*, 731-740.
Wang, Y., Yang, F., Gritsenko, M.A., Clauss, T., Liu, T., Shen, Y., Monroe, M.E., Lopez-Ferrer, D., Reno, T., Moore, R.J.*, et al.* (2011). Reversed-phase chromatography with multiple fraction concatenation strategy for proteome profiling of human MCF10A cells. Proteomics *11*, 2019-2026.